

Distinguishing the impact and signature of black holes from different origins in early cosmic history

Saiyang Zhang,^{1,2}★ Boyuan Liu,³ and Volker Bromm^{1,2,4}

¹*Department of Physics, University of Texas, Austin, TX 78712, USA*

²*Weinberg Institute for Theoretical Physics, University of Texas, Austin, TX 78712, USA*

³*Institute of Astronomy, University of Cambridge, Madingley Road, Cambridge, CB3 0HA, UK*

⁴*Department of Astronomy, University of Texas, Austin, TX 78712, USA*

Accepted XXX. Received YYY; in original form ZZZ

ABSTRACT

We semi-analytically model the effects of primordial black hole (PBH) accretion on the cosmic radiation background during the epoch of reionization ($z \gtrsim 6$). PBHs in the intergalactic medium (IGM) and haloes, where star formation can occur, are considered. For stars with a mass $\gtrsim 25 M_{\odot}$, formed in suitable host haloes, we assume they quickly burn out and form stellar remnant black holes (SRBHs). These SRBHs, like PBHs, also accrete material, and are considered to have similar radiation feedback in the halo environment. To improve the background radiation estimation, we consider the impact of PBHs on structure formation, allowing a modified halo mass function. We consider the radiation feedback from a broad suite of black holes: PBHs, SRBHs, high-mass X-ray binaries (HMXBs), and supermassive black holes (SMBHs). The result shows that at $z \gtrsim 30$, the radiation background energy density is generated by PBHs accreting in the IGM, whereas at lower redshifts, halo accretion dominates. We also dissect the total power density by modeling the accretion spectral energy distribution (SED) across different wavebands. In the UV band, we find that for $f_{\text{PBH}} \lesssim 10^{-3}$, the H-ionizing and Lyman- α fluxes from PBH accretion feedback do not violate existing constraints on the timing of reionization, and on the effective Wouthuysen-Field coupling of the 21-cm spin temperature of neutral hydrogen to the IGM kinetic temperature. However, in the X-ray band, with the same abundance, PBHs contribute significantly and could explain the unresolved part of the cosmic X-ray background.

Key words: dark matter – black hole physics – large-scale structure of Universe – early Universe – cosmic background radiation – accretion, accretion discs

1 INTRODUCTION

Dark matter (DM) has been a long-standing mystery in astrophysical cosmology (e.g. Feng 2010). Although it comprises a significant portion of the cosmic mass-energy density, we still have no knowledge of its micro-physical nature and origin. Whereas most explanations invoke extensions of the standard model of particle physics (e.g. Bertone et al. 2012), an alternative DM scenario is based on primordial black holes (PBHs), formed via the collapse of overdense regions in the early Universe, prior to matter-radiation equality (Zel'dovich & Novikov 1967; Hawking 1971; Sureda et al. 2021). The recent detection of gravitational wave (GW) events (Abbott et al. 2016; Abbott et al. 2020) from merging binary black holes (BBHs) has triggered a new wave of interest in PBHs. In particular, the detection of BBH merger events with total mass $\sim 150 M_{\odot}$ (Abbott et al. 2020) challenges current stellar evolution models (e.g. Liu & Bromm 2020b), raising the possibility of a primordial origin (e.g. Bird et al. 2016; Kashlinsky 2016; Clesse & García-Bellido 2017; De Luca et al. 2020c,d).

However, it is unlikely that PBHs within the mass range $M_{\text{PBH}} \sim 1 - 100 M_{\odot}$, typical for stars and their remnants, provide all of the

cold dark matter (CDM) measured in the Universe, based on multiple empirical constraints (e.g. Carr & Kühnel 2020). Their contribution can be expressed as $f_{\text{PBH}} = \Omega_{\text{PBH}}/\Omega_{\text{DM}}$, the ratio of mass fraction in PBH DM to the total CDM. A prominent observational signature is the GW signal generated from mergers of BBHs. The statistical study of BH merger rates captured by the LIGO-Virgo-KAGRA network (LVK; Ali-Haïmoud et al. 2017; Abbott et al. 2021) constrains the abundance of PBHs to within $f_{\text{PBH}} \lesssim 0.1 - 10^{-3}$. Furthermore, the non-detection of the stochastic gravitational wave background (SGWB) by LVK gives a similar but weaker constraint of $f_{\text{PBH}} \lesssim 0.1$ (Vaskonen & Veermäe 2020; Bagui & Clesse 2022). The recent evidence for a SGWB from pulsar timing array data (e.g. Agazie et al. 2023) implicates a cosmological population of supermassive black hole (SMBH) binaries, and provides promising constraints on supermassive PBHs ($f_{\text{PBH}} \lesssim 0.01$) as well (e.g. Acuña & Tseng 2023; Gouttenoire et al. 2023).

Even though stellar-mass and supermassive PBHs only make up a small fraction of dark matter, they can play important roles in early cosmic history. One of the main physical processes that could affect cosmic evolution is PBH accretion, as the focus of this paper. When PBHs travel through gaseous environments, by the pull of their gravitational well, they will attract and accrete the surrounding gas. In this study, for most cases, we will assume steady accretion of gas onto

★ E-mail: szhangphys@utexas.edu

BHs, as found in Bondi (1952). The accreted gas will lose potential energy and emit the heat generated during this process. The resulting feedback radiation will affect the surrounding medium that PBHs are located in (e.g. Takhistov et al. 2022), and will change the overall cosmic thermal history (e.g. Mena et al. 2019). More specifically, multiple studies show that the energy feedback from this accretion will contribute to cosmic radiation backgrounds at different wavebands (e.g. Ali-Haïmoud & Kamionkowski 2017; Inoue & Kusenko 2017; De Luca et al. 2020a, 2022b; Cappelluti et al. 2022; Ziparo et al. 2022). The change in cosmic microwave background (CMB) power spectra derived from PBH accretion limits their abundance, where stellar-mass PBHs are found to comprise no more than a small fraction of DM, $f_{\text{PBH}} \lesssim 0.1 - 10^{-3}$ (e.g. Poulin et al. 2017; Serpico et al. 2020), similar to the constraints derived from GW observations. Further constraints from accretion onto PBHs are summarized in Carr et al. (2021).

Moreover, with the recently launched JWST, observing in the near-infrared (NIR) electromagnetic (EM) wave band [0.7 – 5 μm], astronomers start to unveil an increasing number of galaxies at $z \gtrsim 12$ (e.g. Finkelstein et al. 2022), discover SMBHs during their early formation stages (e.g. Natarajan et al. 2017; Larson et al. 2023), and aim to study anisotropies in the cosmic near-infrared background (CIB; Kashlinsky et al. 2015; Helgason et al. 2016). Some of the galaxies, if confirmed by spectroscopic follow-up, are so massive that they could challenge the standard ΛCDM model of cosmological structure formation (Labbé et al. 2023; Boylean-Kolchin 2023). PBHs can potentially address these latest observations in a broader context with their effects on the matter power spectrum and the subsequent structure formation history, as well as on the halo mass distribution (e.g. Afshordi et al. 2003; Carr & Silk 2018; Kashlinsky 2021; Atrio-Barandela 2022; Liu & Bromm 2022a). This change to the halo mass function will also affect the total accretion feedback from PBHs located in haloes, and consequently the cosmic radiation background generated by the aggregate emission (Kashlinsky 2016; Cappelluti et al. 2022; Liu et al. 2022).

In this paper, we will assess the impact of PBHs in the mass range $M_{\text{PBH}} \sim 1 - 100 M_{\odot}$ on early cosmic history, considering all BHs generated from different mechanisms as possible power sources contributing to the cosmological background radiation. We will consider the redshift range $z \sim 100 - 6$, starting from an almost homogeneous matter distribution to the end of reionization. Overall, we will divide our treatment into PBHs floating in the intergalactic medium (IGM), and those residing in DM haloes. Calculating the resulting feedback energy from the accretion of the surrounding gas, in the former case we consider the effects of Hubble flow and Compton scattering, which will effectively slow down the accretion process (see Ricotti 2007; Ricotti et al. 2008). For the latter case, for simplicity, we assume that PBHs sit near the center of the halo following an isothermal density profile, as previously simulated in Liu et al. (2022). In addition, we consider astrophysical BHs generated from the death of massive stars ($\gtrsim 30 M_{\odot}$) in virialized haloes (e.g. Husain et al. 2021), as well as SMBHs in more massive haloes with $M_{\text{h}} \gtrsim 10^8 M_{\odot}$ (e.g. Jeon et al. 2022). This broad suite of accreting BHs in the early Universe is likely contributing to the sources for the unresolved part of the fluctuations in the cosmic X-ray and infrared backgrounds (CXB/CIB), as summarized in the review by Kashlinsky et al. (2018).

A similar topic has been discussed in recent works (Cappelluti et al. 2022; Ziparo et al. 2022), where the radiation background from PBH accretion has been evaluated. However, different from the assumptions of those studies, we will focus on the radiation background contribution from all BH sources, including stellar-remnant

black holes (SRBHs), such as high-mass X-ray binaries (HMXBs). Therefore, we will integrate over haloes with a broad mass range of $\sim 10^5 - 10^{13} M_{\odot}$, whereas Ziparo et al. (2022) only considered mini-haloes without star formation ($\lesssim 10^7 M_{\odot}$). Also, we will consider the case of enhanced accretion by PBH-seeded DM haloes within the IGM, whereas Cappelluti et al. (2022) only considered PBH accretion in star-forming haloes. With our new implementations, we will reach a broader understanding of the PBH-feedback-generated radiation backgrounds.

The structure of our paper is as follows. Section 2 will address the impact of PBHs on structure formation and introduce the different sources of black holes, to be considered in the following treatment. In Section 3, we will discuss the accretion physics in the IGM and DM haloes separately. Subsequently, we derive the resulting generation of radiation and heat, assessing the corresponding observational signatures in Section 4. We summarize and offer conclusions in Section 5. Throughout this paper, we adopt a PBH-DM ΛCDM cosmology with parameters: $\Omega_{\text{m}} = 0.3153$, $\Omega_{\text{b}} = 0.04930$, $n_{\text{s}} = 0.96$, and $h = 0.6736$ (Planck Collaboration et al. 2020). The density fraction of CDM is then given by: $\Omega_{\text{DM}} = \Omega_{\text{m}} - \Omega_{\text{b}}$, with a possible PBH sub-component of $\Omega_{\text{PBH}} = f_{\text{PBH}}\Omega_{\text{DM}}$.

2 BLACK HOLES IN THE EARLY UNIVERSE

In this section, we will address the overall cosmic evolution at high redshifts in the presence of PBHs, as summarized in Figure 1, where we display the entire suite of BHs from different origins. First, in Section 2.1, we briefly summarize previous results on how cosmological structure formation is modified by PBH DM, including changes to the halo mass function, as compared to standard ΛCDM . Then, in Section 2.2, we touch on select PBH formation mechanisms and the resulting mass distribution. We similarly discuss relevant aspects for BHs of astrophysical origins in Section 2.3.

2.1 Cosmological Structure Formation

Following the general formalism introduced in previous work (Afshordi et al. 2003; Inman & Ali-Haïmoud 2019), we consider density perturbations as a function of redshift z , consisting of adiabatic and isocurvature terms, $\delta_{\text{ad}}(z)$ and $\delta_{\text{iso}}(z)$, respectively. Adiabatic perturbations uniformly affect all mass-energy components, such that $\delta_{\text{ad}}(z)$ applies to all forms of DM. In this context, the isocurvature term derives from the discreteness of individual PBHs (Kashlinsky 2016; Desjacques & Riotto 2018; De Luca et al. 2020d), and can be written as

$$\delta_{\text{iso}}(\mathbf{x}) \equiv \frac{\delta\rho_{\text{PBH}}}{\bar{\rho}_{\text{DM}}} = \frac{f_{\text{PBH}}}{\bar{n}_{\text{PBH}}} \sum_i \delta_D(\mathbf{x} - \mathbf{x}_i) - 1. \quad (1)$$

Here, δ_D is the Dirac delta function, \mathbf{x}_i marks the position of the i -th PBH, and \bar{n}_{PBH} is the average PBH number density, which depends on the average PBH mass. This formalism can be extended to a broader mass spectrum, with a characteristic mass scale of M_{c} , as stated in, e.g., Carr (1975); Choptuik (1993). In general, we thus write the average density as

$$\bar{n}_{\text{PBH}} = \frac{f_{\text{PBH}}}{M_{\text{c}}} \Omega_{\text{DM}} \frac{3H_0^2}{8\pi G}. \quad (2)$$

Given the limits on the abundance of PBHs, implying that they do not compose the totality of DM, we assume that the remainder of (cold) DM is provided by particle DM (PDM). We thus consider an additional term imprinted by the PBH isocurvature perturbations on

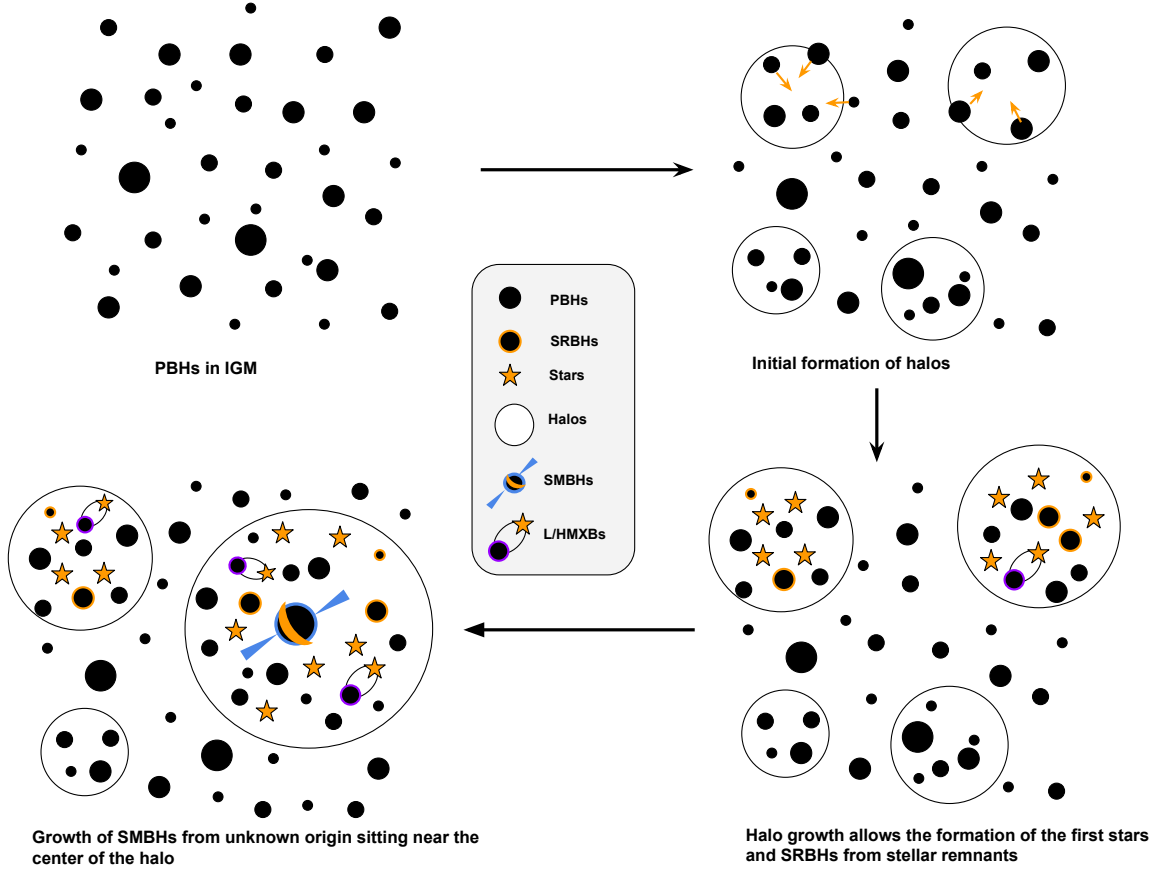


Figure 1. Overall role of PBHs in early cosmic evolution. Initially, before the onset of structure formation, PBHs reside in the quasi-homogeneous intergalactic medium (IGM), as shown in the **top left panel**. As the Universe expands and cools, haloes of small masses ($\sim 10^5 - 10^6 M_\odot$) start to emerge from the gravitational instability, and PBHs cluster in those minihaloes, as illustrated in the **top right panel**. As haloes keep growing, the first stars form in sufficiently massive haloes from the collapse of primordial gas clouds. Stars with mass below the pair-instability limit ($\sim 10 - 130 M_\odot$) quickly die and collapse into stellar-remnant black holes (SRBHs). In certain cases, some of the stars form in binaries, where the more massive component becomes a black hole. Through accretion from the companion star, the black hole emits strong X-rays, giving rise to low/high mass X-ray binaries (L/HMXBs), depending on the mass of the BH (see the **lower right panel**). As some of the haloes have grown increasingly massive, in excess of $\gtrsim 10^8 M_\odot$, the black hole in the center of the galactic bulge starts to accrete at nearly Eddington rate to grow into supermassive black holes (SMBHs), which exert vigorous radiative feedback during this process. This more complex stage in cosmic evolution, with the full panoply of BH sources, is summarized in the **lower left panel**.

the PDM, such that the combined evolution of the density perturbations in both DM (PDM) and PBHs is given as follows:

$$\begin{aligned} \delta_{\text{DM}}(z) &= \delta_{\text{ad}}(z) + \delta_{\text{iso}}(z) = \delta_{\text{ad}}(z) + [T_{\text{iso}}(z) - 1] f_{\text{PBH}} \delta_{\text{iso}}^0, \\ \delta_{\text{PBH}}(z) &= \delta_{\text{DM}}(z) + \delta_{\text{iso}}^0 = \delta_{\text{ad}}(z) + T_{\text{iso}}^{\text{PBH}}(z) \delta_{\text{iso}}^0. \end{aligned} \quad (3)$$

The evolution of adiabatic perturbations with respect to z is expressed via $\delta_{\text{ad}}(z) = T_{\text{ad}}(z) \delta_{\text{ad}}^0$. Here, δ_{ad}^0 and δ_{iso}^0 correspond to the primordial adiabatic and PBH isocurvature perturbations, whereas $T_{\text{ad}}(z)$ and $T_{\text{iso}}(z)$ are the linear transfer functions for the two modes, both normalized to 1 as $z \rightarrow \infty$. The perturbation in PDM induced by PBHs is $\delta_{\text{iso}}(z) = [T_{\text{iso}}(z) - 1] f_{\text{PBH}} \delta_{\text{iso}}^0$, and we can write the transfer function for PBH-induced isocurvature fluctuations as $T_{\text{iso}}^{\text{PBH}}(z) = 1 + [T_{\text{iso}}(z) - 1] f_{\text{PBH}}$. We note that the transfer function is in turn related to the structure growth factor, $T(z) = D(z)$. To a good approximation, we can use the results from solving the cosmic fluid equations with embedded point masses (Meszaros 1974), and adopt the following analytical fit for the growth factor (Inman &

Ali-Haïmoud 2019):

$$\begin{aligned} D(z) &\approx \left(1 + \frac{3\gamma}{2\alpha_-} s\right)^{\alpha_-}, \quad s = \frac{1 + z_{\text{eq}}}{1 + z} \\ \gamma &= \frac{\Omega_m - \Omega_b}{\Omega_m}, \quad \alpha_- = \frac{1}{4}(\sqrt{1 + 24\gamma} - 1), \end{aligned} \quad (4)$$

where $z_{\text{eq}} \sim 3400$ represents the redshift at matter-radiation equality. Since we restrict our treatment to the matter-dominated era with $z \ll z_{\text{eq}}$, we have $s \gg 1$ ($z \rightarrow 0$). Therefore, $D_{\text{iso}} \approx 3s/2$ (assuming $\gamma \approx 1$ and $\alpha_- \approx 1$ to be constant).

Given the two-point correlation function for the density perturbations from PBH DM:

$$\langle \delta_{\text{PBH}}(\mathbf{x}) \delta_{\text{PBH}}(\mathbf{0}) \rangle = \frac{f_{\text{PBH}}^2}{\bar{n}_{\text{PBH}}} \delta_D(\mathbf{x}) + \xi_{\text{PBH}}(x), \quad (5)$$

where $\xi_{\text{PBH}}(x)$ represents the reduced correlation function as a function of separation distance $x = |\mathbf{x}|$ (e.g. Chisholm 2006; Desjacques & Riotto 2018; Dizgah et al. 2019; De Luca et al. 2022a), we can calculate the power spectrum by taking the spatial Fourier transform of the correlation function of all perturbation modes. Specifically, the isocurvature term $P_{\text{iso}}(k)$ from PBHs approximates to

$f_{\text{PBH}}^2/\bar{n}_{\text{PBH}}$. We can then express the total power spectrum¹ at $z = 0$ as follows:

$$P_{\text{tot}}(k) = P_{\Lambda\text{CDM}}(k) + P_{\text{iso}}(k), \quad (6)$$

$$P_{\text{iso}}(k) = [f_{\text{PBH}}D_0]^2 / \bar{n}_{\text{PBH}} + T_{\text{mix}}^2(k)P_{\Lambda\text{CDM}}(k).$$

Initially, the adiabatic and iso-curvature modes are not correlated. However, at a later stage ($z \sim 10$), we need to consider the correlation between the isocurvature and adiabatic perturbations since PBHs are more abundant in overdense regions on larger scales, but disrupt DM structure around them on smaller ones. Here, similar to the prescription in Liu et al. (2022), we introduce a mode mixing term governed by the transfer function T_{mix} . Considering the inter-PBH separation scale, $k_{\text{PBH}} = (2\pi^2\bar{n}_{\text{PBH}})^{1/3}$, we use the heuristic formula calibrated to simulation results in Liu et al. (2022):

$$T_{\text{mix}}^2(k) = \begin{cases} f_{\text{PBH}}D_0^2D_{\text{ad},0}^{-1}(k/k_{\text{PBH}})^3, & k \leq 3k_{\text{PBH}} \\ 0, & k > 3k_{\text{PBH}} \end{cases}, \quad (7)$$

where $D_0 = D(z=0)$ is the growth factor for the isocurvature mode, and $D_{\text{ad},0} = D_{\text{ad}}(z=0)/D_{\text{ad}}(z=z_{\text{eq}})$ for the adiabatic mode², both evaluated at redshift 0.

From the total power spectrum, we calculate the density contrast as a function of the window mass M :

$$\sigma(M) = \left[\frac{1}{2\pi^2} \int P_{\text{tot}}(k)W_{\text{TH}}(kr_M)k^2dk \right]^{1/2}, \quad (8)$$

where $W_{\text{TH}}(kr_M)$ is the top-hat Fourier transform of the spherical window function, and r_M corresponds to the comoving radius associated with the mass window M . We note that for non-linear scales, where $\sigma(M) \gtrsim 1$, this mass corresponds to a virialized halo structure. Therefore, in the following, we will assume $M_h = M$ for the halo mass. Employing the Press-Schechter formalism for the halo distribution (Press & Schechter 1974)³, the number density of virialized structures (halo mass function) between M_h and $M_h + dM_h$ is:

$$n(M_h, z)dM_h = \sqrt{\frac{2}{\pi}} \frac{\bar{\rho}}{M_h^2} \frac{\delta_c(z)}{\sigma(M_h)} \times \exp\left(-\frac{\delta_c^2(z)}{2\sigma^2(M_h)}\right) \left| \frac{d \ln \sigma(M_h)}{d \ln M_h} \right| dM_h, \quad (9)$$

where $\bar{\rho}$ is the average comoving matter density, and the critical overdensity factor, $\delta_c(z)$, as a function of redshift is given by

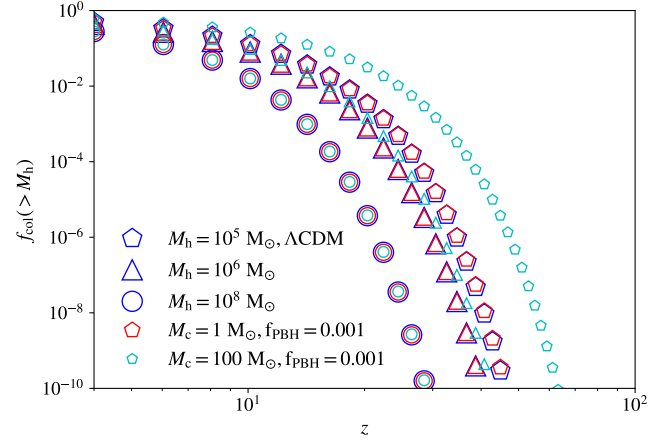
$$\delta_c(z) \simeq \frac{1.686}{D_{\text{ad}}(z)}. \quad (10)$$

Integrating the halo number density over the mass range of interest

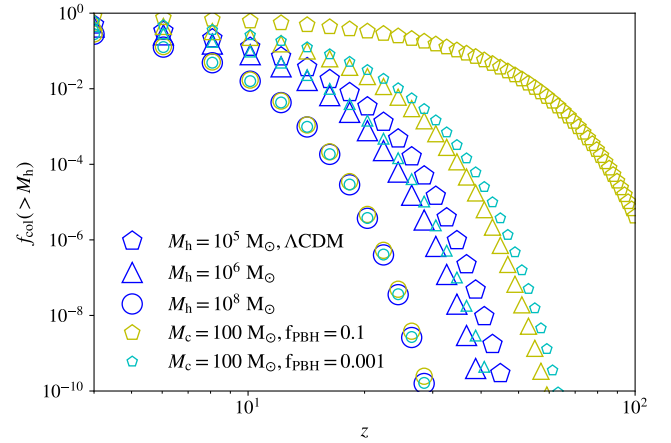
¹ In our calculation, we have used the package Colossus (Diemer 2018) to generate the ΛCDM power spectrum, $P_{\Lambda\text{CDM}}(k)$, as calibrated by Planck Collaboration et al. (2020).

² We denote the growth factor of the adiabatic mode as $D_{\text{ad}}(z)$, and adopt the semi-analytical fit from Equ.(4.74)-(4.76) in Mo et al. (2010).

³ We note that the effect of PBH clustering at smaller scales, mainly represented by $\xi_{\text{PBH}}(x)$, will contribute to the non-Gaussian part of the density field (e.g. Chisholm 2006; Desjacques & Riotto 2018; Kashlinsky 2016; Atrio-Barandela 2022). Our use of the standard Press-Schechter formalism here thus is a simplification, approximating the halo abundance. Another simulation study will be needed, in continuation of Liu et al. (2022), to fully address the effect of PBH clustering.



(a) Constant mass fraction $f_{\text{PBH}} = 0.001$, but considering changes in mass scale: $M_c = 1 M_{\odot}$ (red) and $100 M_{\odot}$ (cyan).



(b) Varying PBH abundance, $f_{\text{PBH}} = 0.1$ (yellow) and 0.001 (magenta), keeping the mass scale constant at $M_c = 100 M_{\odot}$.

Figure 2. Collapse fraction in haloes larger than 10^5 (pentagon), 10^6 (triangle), and $10^8 M_{\odot}$ (circle), vs. redshift z . Here, we consider the changes in the formation of structures in the presence of PBHs (red, cyan and yellow, compared to the standard ΛCDM case (blue)).

and dividing by the average mass density, the collapse fraction of the cosmic matter is given by

$$f_{\text{col}}(> M_h|z) = \frac{1}{2} \text{erfc}\left(\frac{\delta_c(z)}{\sqrt{2}\sigma(R)}\right), \quad (11)$$

and is plotted in Figure 2.

As can be seen, in the presence of PBHs, more minihaloes ($M_h \sim 10^5 M_{\odot}$) form than in the standard ΛCDM case. Also, the abundance of minihaloes will depend on the characteristic PBH mass, M_c , but more strongly on the PBH abundance. This behaviour can be explained by the shift of total power spectrum P_{tot} in the presence of PBHs by the isocurvature term $f_{\text{PBH}}^2/\bar{n}_{\text{PBH}}$ in Equ. (6), which changes the density contrast subsequently. In addition, we have examined the effect of the mode mixing term in Equ. (7), finding that it does not significantly change the collapse fraction within the PBH mass scale considered here. However, as we increase the mass scale to $\gtrsim 100 M_{\odot}$, minihaloes of mass $\lesssim 10^6 M_{\odot}$ would be less abundant, if mode mixing were excluded. Going forward, the collapse fraction allows us to calculate the PBH abundance in the IGM, whereas the

halo mass function enables us to evaluate the prevalence of PBHs in DM haloes.

2.2 Primordial Black Holes

Several previous works provide reviews of the PBH formation mechanisms and abundance constraints from phenomenological studies (e.g. Carr & Kühnel 2020; Carr et al. 2021; Escrivà et al. 2023). In this paper, we consider PBHs with different mass distributions and study how these changes affect the radiation background output. To begin, the PBH mass distribution $\psi(M_{\text{PBH}})$ with respect to PBH mass M_{PBH} is related to the differential number density as follows:

$$\frac{dn_{\text{PBH}}}{d \ln M_{\text{PBH}}} = f_{\text{PBH}} \Omega_{\text{DM}} \frac{3H_0^2}{8\pi G} \psi(M_{\text{PBH}}). \quad (12)$$

Here, $\psi(M_{\text{PBH}})$ is the mass probability distribution function, normalized to 1 when integrating over $\ln M_{\text{PBH}}$, and it reflects the specific PBH formation mechanism. In the most common scenario, PBHs follow a monochromatic mass distribution when all PBHs form from the collapse of overdensities during the radiation-dominated era (e.g. Carr 1975). The mass function then takes the simple form:

$$\psi(M_{\text{PBH}}) = \delta(M_{\text{PBH}} - M_c), \quad (13)$$

where M_c is the characteristic PBH mass scale.

Another scenario suggests that PBHs form in smooth peaks of the inflation power spectrum, generating an initial mass function with a lognormal shape (Dolgov & Silk 1993). The functional form is given by:

$$\psi(M_{\text{PBH}}) = \frac{1}{\sqrt{2\pi}\sigma M_{\text{PBH}}} \exp\left(-\frac{\ln^2(M_{\text{PBH}}/M_c)}{2\sigma^2}\right), \quad (14)$$

where σ denotes the width of the PBH distribution. Constraints on the parameter space (f_{PBH} , σ , M_c) for the lognormal distribution have been calculated in Kühnel & Freese (2017), specifically concluding that $0 < \sigma \leq 1$. We note that as $\sigma \rightarrow 0$, the lognormal distribution reduces to the monochromatic distribution. We also note that many other shapes of PBH mass functions are discussed in the literature, like the power-law or critical collapse functions (Carr et al. 2021). Here, we mostly restrict our attention to the monochromatic mass function, but our calculation also applies to lognormal distributions with a narrow dispersion. A comprehensive investigation with respect to different shapes of the initial PBH mass function will require another study.

2.3 Astrophysical Black Holes

2.3.1 Supermassive Black Holes

We will consider SMBHs as powerful sources of radiation in difference from other astrophysical black holes. For a comprehensive discussion of the formation and impact of SMBHs, we refer the reader to recent reviews (e.g. Smith & Bromm 2019; Inayoshi et al. 2020). Our focus here is on the mass relationship between the SMBH and its host halo. For the sake of our analysis, we operate under the optimistic⁴ assumption that SMBHs are located at the center of all

massive haloes with $M_h \gtrsim 10^8 M_\odot$. This assumption allows us to directly derive the SMBH mass function from the halo mass function. Specifically, the mass of the central black hole is related to that of its host halo, as follows:

$$M_{\text{SMBH}} = \eta(M_h, z) M_h, \quad (15)$$

where the BH formation efficiency, $\eta(M_h, z)$, is a function of halo mass and redshift. In Jeon et al. (2022), it is calculated using a global energy balance argument as:

$$\eta \simeq 2 \times 10^{-7} \left(\frac{1+z}{10}\right) \left(\frac{f}{0.1}\right)^{-1} \left(\frac{M_h}{10^{10} M_\odot}\right)^{2/3}, \quad (16)$$

where f is the fraction of the BH rest mass energy deposited into the host halo gas as heat. However, this idealized formalism scales as $\eta \propto (1+z)$, and it does not converge to 0 at high redshifts ($z \gtrsim 15$), where SMBHs begin to form. Therefore, we also adopt the fitted value of $\eta(M_h, z)$ provided by the UNIVERSE MACHINE, which is based on observational data (Zhang et al. 2023). This is discussed in more detail in Appendix A.

2.3.2 Isolated Black Holes from Stellar Remnants

We also consider stellar-remnant black holes (SRBHs) as the eventual product of the stellar evolution. The resulting abundance of SRBHs hinges on modeling of both the underlying stellar evolution and star-formation history. To proceed, we need to apply constraints on BHs derived from their progenitor stars. The eventual fate of a single star with an initial mass M_i can be summarized as follows (Heger et al. 2003):

- $M_i < 10 M_\odot \rightarrow$ white dwarf
- $10 M_\odot < M_i < M_{\star,c} \rightarrow$ neutron star
- $M_{\star,c} < M_i < 140 M_\odot \rightarrow$ black hole
- $140 M_\odot < M_i < 260 M_\odot \rightarrow$ pair-instability supernova (PISN)
- no remnant
- $M_i > 260 M_\odot \rightarrow$ massive black hole

Here, $M_{\star,c}$ is the critical mass, before mass loss, above which a single star will eventually produce a BH, with a value of approximately $25 M_\odot$. According to Heger et al. (2003), the products of stellar evolution also depend on the metallicity of the stars. For extremely low metallicity stars, such as Population III (Pop III) stars, the summary above accurately captures the fate of dying stars. However, for higher metallicity Pop I/II stars with $Z \gtrsim 10^{-4} Z_\odot$, where mass loss is expected to be severe, the PISN stage of evolution may never occur, and is replaced by a BH remnant fate. Therefore, we assume that all Pop I/II stars with an initial mass larger than the critical mass will evolve into BHs.

The literature offers various forms for the initial mass function (IMF) for different stellar populations, often characterized by a single or broken power-law (e.g. Chabrier 2003). Since our primary focus here is on the more massive stars that have the potential to form BHs, we adopt a simple power law for the stellar IMF:

$$\frac{dN}{dM_i} = C M_i^\alpha, \quad (17)$$

where C is a normalization constant. For simplicity, we assume that any BH with a progenitor mass larger than $260 M_\odot$ contributes to the SMBH mass budget, and is thus implicitly accounted for in the SMBH tally. For simplicity, we assume a universal lower cutoff for the stellar mass, independent of metallicity, such that $M_{i,\text{min}} = 0.1 M_\odot$ and $M_{i,\text{max}} = 260 M_\odot$ represent the minimum and maximum stellar

⁴ Recent JWST observations have discovered a population of active galactic nuclei (AGN) at $z \gtrsim 5$ with a much higher abundance than previously expected, which implies a surprising ubiquity of SMBHs in high- z galaxies (e.g. Furtak et al. 2023; Greene et al. 2024; Harikane et al. 2023b; Kocevski et al. 2023; Maiolino et al. 2023; Matthee et al. 2023). Motivated by this discovery, we assume that all haloes above a certain mass threshold host SMBHs.

mass for our idealized IMF, respectively. Integrating, we obtain the total stellar mass:

$$M_{\star} = \int_{M_{i,\min}}^{M_{i,\max}} \left(\frac{dN}{dM_i} \right) M_i dM_i \quad (18)$$

in turn determining the normalizing constant. Here, we will consider both top-heavy ($\alpha = -1.35$; Stacy & Bromm 2013) and Salpeter ($\alpha = -2.35$; Salpeter 1955) IMF slopes for Pop III stars, but only the Salpeter value for Pop I/II stars. Given the stellar mass function, a rough estimate for the BH mass function is:

$$\left(\frac{dN}{dM_{\text{SRBH}}} \right) = \left(\frac{dN}{dM_i} \right) \frac{dM_i}{dM_{\text{SRBH}}}. \quad (19)$$

The derivative of the initial-to-remnant (SRBH) mass relation is evaluated by interpolating figure 2 from Husain et al. (2021). In the case of PISNe, for stars with an initial mass larger than $140 M_{\odot}$ or smaller than the critical mass $M_{\star,c}$, this function will return 0.

Overall, the total stellar BH mass in a halo of mass M_h at a given redshift can be estimated by integrating over the halo star formation history (SFH), as follows:

$$M_{\bullet,\text{tot}}(M_h, z) = \int_{z_{\text{ini}}}^z \text{SFH}(M_h, z') f_{\text{loss}}(t(z) - t(z')) |M_i \geq M_{\star,c} \times f_{\text{rem}}(t(z) - t(z')) \left| \frac{dt}{dz'} \right| dz'. \quad (20)$$

In the above expression, $f_{\text{loss}}(t|M_i \geq M_{\star,c})$ denotes the mass fraction of the stellar population contained in stars with initial masses exceeding the critical mass $M_{\star,c}$ that have lifetimes shorter than t . This fraction is a function of the time difference between the current redshift z and the redshift z' at which the stars initially form. Since there is still uncertainty regarding the onset of first star formation (e.g. see fig. 2 in Klessen & Glover 2023), for definiteness, we assume that Pop III star formation begins at $z_{\text{ini}} = 50$.

We note that the lifetime of the massive stars ($\geq 10 M_{\odot}$) capable of forming BHs is less than $\sim \mathcal{O}(10 \text{ Myr})$. Therefore, the fraction $f_{\text{loss}}(t|M_i > M_{\star,c})$ will reach the maximum at $t \geq 10 \text{ Myr}$. Since in most cases, the cosmic time difference between the moment of star formation (z') and a given reference redshift (z) will be $\gg 10 \text{ Myr}$, we remove the time dependence and approximate f_{loss} with its final maximum value for simplicity⁵:

$$f_{\text{loss}} \simeq \frac{\int_{M_{\star,c}}^{M_{i,\max}} \left(\frac{dN}{dM_i} \right) M_i dM_i}{M_{\star}}. \quad (21)$$

In Equation (20), f_{rem} signifies the fraction of the progenitor star's mass converted into (astrophysical) BH remnants, given by the ratio of the final BH mass, M_{SRBH} , to the initial stellar mass, M_i . Upon integrating over the relevant mass interval, we arrive at the remnant mass fraction, as follows:

$$f_{\text{rem}} \simeq \frac{\int_{M_{\star,c}}^{M_{i,\max}} \left(\frac{dN}{dM_i} \right) M_{\text{SRBH}}(M_i) dM_i}{\int_{M_{\star,c}}^{M_{i,\max}} \left(\frac{dN}{dM_i} \right) M_i dM_i}. \quad (22)$$

To model the star-formation history in a halo at redshift z , we separately consider the formation history of Pop III and Pop

⁵ As noted earlier, the upper mass limit for this integration depends on the stellar population. The maximum BH progenitor mass, $M_{\text{SRBH,max}}$, is $140 M_{\odot}$ for Pop III stars and $260 M_{\odot}$ for Pop I/II stars.

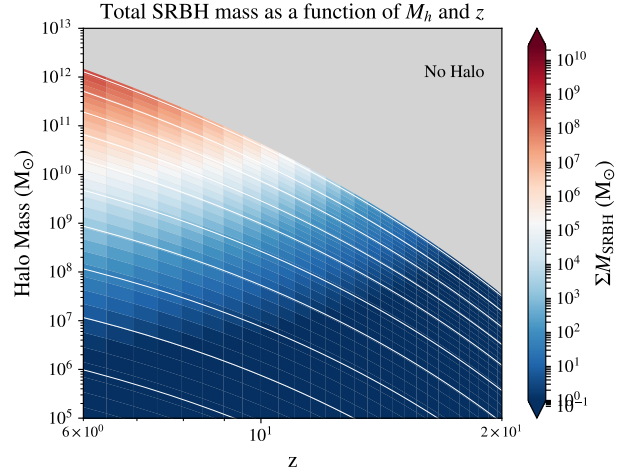


Figure 3. Cumulative BH mass from star formation throughout cosmic history. The overall star formation rate was generated by the parametric fit from the UNIVERSE MACHINE (Zhang et al. 2023). We explicitly add Pop III star formation as the dominant contribution at high redshifts ($z \geq 15$) (Liu & Bromm 2020a). The grey area represents the effective absence of star forming haloes, with negligible halo number densities at those redshifts. The white lines reproduce the halo mass growth histories of select haloes.

I/II stars as a function of redshift, represented as $\text{SFH}(M_h, z) = \text{SFH}_{\text{III}}(M_h, z) + \text{SFH}_{\text{I/II}}(M_h, z)$. In a first order approximation, we can express this as the product of the comoving volume corresponding to a given halo, and the comoving cosmic star formation rate density (SFRD):

$$\text{SFH}_i(M_h(z), z) = \text{SFRD}_i(z) \times V_c(M_h(z), z). \quad (23)$$

Here, $V_c(M_h(z)) = 8\pi G M_h(z) / 3H_0^2$ represents the comoving volume corresponding to the halo mass $M_h(z)$, and the subscript i refers to the specific population of stars.

We note that the SFRD is an average over cosmological volumes, and is thus not accurately representing the conditions in a given halo. Star formation is dominated by Pop I/II stars at redshift $z \lesssim 10$, a phenomenon well-constrained by available data (for a recent review, see Klessen & Glover 2023). Accordingly, we employ the fit from the Universe Machine (Behroozi et al. 2013) for the formation history of Pop I/II stars, denoted as $\text{SFH}_{\text{I/II}}(M_h, z)$. The parametric fit, along with the SMBH masses, are summarized in Appendix A. However, the formation rate at $z \geq 10$ remains largely uncertain due to the scarcity of available data, and the fit from the Universe Machine predicts almost no star-formation within minihaloes. As such, we use the fit for Pop III SFRD based on a cosmological simulation presented in Liu & Bromm (2020a), rephrased for the typical redshift $z \sim 20$ of Pop III star formation:

$$\frac{\text{SFRD}_{\text{III}}(z)}{M_{\odot} \text{yr}^{-1} \text{Mpc}^{-3}} = 1.1 \times 10^{-5} \frac{[(1+z)/21]^{2.63}}{0.054 + [(1+z)/21]^{8.55}}. \quad (24)$$

Evaluating Equ. (20-24), we arrive at Figure 3, which summarizes the total mass of SRBHs as a function of redshift and halo mass. We observe that, generally, as the mass of the dark matter (DM) halo increases, more astrophysical black holes (SRBHs) are produced. Moreover, the total BH mass approximately scales as $\sim 10^{-4} M_h$ at $z \simeq 6$.

On the other hand, we also consider two separate fits, namely Madau & Dickinson (2014) and Harikane et al. (2022), for the total star formation rate density (SFRD) as a first-order approximation to the star formation history (SFH) of Pop I/II stars in a galaxy using

Equ. (23). Recent studies have found these two fits to be reasonable bounds for the observed SFRD of galaxies at $z = 9 - 16$ (Harikane et al. 2023a), with the work by Madau & Dickinson (2014) serving as the upper bound. Therefore, at $z \geq 10$, we can express the upper bound and extrapolate it to even higher redshifts as follows:

$$\frac{\text{SFRD}_{\text{I/II}}(z)}{M_{\odot}\text{yr}^{-1}\text{Mpc}^{-3}} \lesssim 0.007 \frac{[(1+z)/10]^{2.7}}{0.001 + [(1+z)/10]^{5.6}} \quad (25)$$

2.3.3 X-ray Binaries

One important source of radiation feedback arises from the remnants of massive stars that form in binaries. Specifically, we focus on high-mass X-ray binaries (HMXBs, reviewed by e.g. Fornasini et al. 2023), where one of the stars in the binary has an initial mass $M_i \gtrsim M_{\star,c}$. To estimate the abundance of HMXBs, we consider the cases of Pop III and Pop I/II stars separately. For Pop III stars, we adopt the prescription from previous studies as described in Jeon et al. (2014) and Stacy & Bromm (2013); Liu et al. (2021), assuming that about $\sim 30\%$ of Pop III stars form in binaries. On the other hand, observations suggest a larger binary fraction of approximately 0.5 in the local universe (e.g. Sana et al. 2013; Clark et al. 2023). Therefore, we apply this factor of 0.5 to Pop I/II stars. We acknowledge that not all massive binaries will evolve into HMXBs due to many factors, such as common envelope evolution and metallicity (e.g. Power et al. 2009; Mirabel et al. 2011). Regarding those massive binary stars, for simplicity, we assume that all of them experience stages of X-ray activity and use a simple phenomenological model to calculate their radiation, thus providing an upper limit for the HMXB production and radiation from the corresponding accretion.

Specifically, we consider a duty cycle during which HMXBs accrete mass and strongly radiate. To bracket the uncertainties, we assign a value of 0.1 – 1 to represent this duty cycle, which has a weak correlation with HMXB luminosity, according to observations (e.g. Sidoli & Paizis 2018). Furthermore, we assign a lifetime of $t_{\text{acc}} \sim 1 - 10$ Myr to all HMXBs to allow them to accrete a substantial amount of mass ($\sim \mathcal{O}(M_{\odot})$) from their companions (Mirabel et al. 2011). We estimate the total mass of active HMXBs in a given halo of mass M_h as follows:

$$\begin{aligned} M_{\text{HMXB}}(M_h, t(z)) / f_{\text{HMXB}} \\ = \int_{t(z)-t_{\text{acc}}}^{t(z)} \text{SFH}(M_h, t') f_{\text{loss}} f_{\text{rem}} dt' \\ \approx \text{SFH}(M_h, t(z)) f_{\text{loss}} f_{\text{rem}} t_{\text{acc}} . \end{aligned} \quad (26)$$

Here, f_{HMXB} refers to the aforementioned fraction of massive stars that form in binaries. The second equality is valid since t_{acc} is much smaller than the cosmic time t . We note that a comprehensive assessment of the energy feedback from HMXBs would require a dedicated study with binary population synthesis (see e.g. Fragos et al. 2013a,b; Sartorio et al. 2023; Liu et al. 2024), beyond the scope of the current paper.

With the prescriptions above and integrating over the halo mass function, we can derive the average BH density for different species and redshifts. An example is shown in Figure 4 for a monochromatic PBH mass distribution with $M_c = 10 M_{\odot}$, and a mass fraction in DM of $f_{\text{PBH}} = 10^{-3}$. We calculated the total mass density of PBHs to be $\sim 10^8 M_{\odot}\text{Mpc}^{-3}$. We conclude that PBHs will dominate the BH mass budget throughout the redshift range considered here, unless $f_{\text{PBH}} \lesssim 10^{-4}$. However, as more stars form and die, around $z \sim 6$, the mass density in SRBHs (including HMXBs) becomes non-negligible in dark matter haloes, at about $\sim 10^{-2}$ times the mass density of the PBHs. Moreover, we notice that the SRBH fraction in the form of

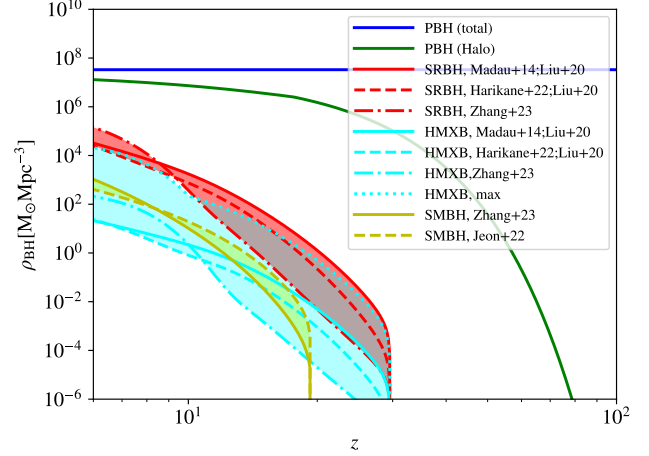


Figure 4. The evolution of BH density from various sources: all PBHs (blue), PBHs in haloes (green), SRBHs (red), HMXBs (blue), and SMBHs (yellow). Here, we show results for a monochromatic PBH mass distribution with $M_c = 10 M_{\odot}$, and a mass fraction in DM of $f_{\text{PBH}} = 10^{-3}$. For SRBHs, we assume instantaneous formation from the remnants of massive stars. To comprehensively calculate the BH mass budget for SRBH and HMXBs, we employ the star formation history of both Pop III and Pop I/II stars (Madau & Dickinson 2014; Liu & Bromm 2020a; Harikane et al. 2022, 2023a; Zhang et al. 2023), assuming a Salpeter IMF for Pop I/II stars, and a top-heavy IMF for Pop III stars. We show the maximum possible HMXB contribution (cyan dotted line), representing the limiting case of full duty cycle and accretion time of ~ 10 Myr. For the other cases, we assign a duty cycle of 0.1 and an accretion time of ~ 1 Myr. For the case of SMBHs, we use the models from Jeon et al. (2022) (dashed) and Zhang et al. (2023) (solid). Here, Mass densities are given in comoving units.

active X-ray binaries is comparable to the abundance of SMBHs, both reaching a mass density level of around $\sim 10^3 M_{\odot}\text{Mpc}^{-3}$, generally consistent with the result from Jeon et al. (2022).

3 ACCRETION PHYSICS

In this section, we briefly describe the BH accretion physics as we aim to study the corresponding energy feedback. We consider BHs of different origins, located either in the intergalactic medium (IGM) (Section 3.1) or in haloes (Section 3.2).

In general, regarding the accretion rate of a BH, we adopt a modified version of the Bondi-Hoyle steady accretion formula (Tremmel et al. 2017):

$$\dot{M}_{\bullet} = \frac{4\pi(GM_{\bullet})^2 \rho_{\text{gas}}}{v_{\text{eff}}^3} = \frac{4\pi(GM_{\bullet})^2 \rho_{\text{gas}}}{(c_s^2 + v_{\text{rel}}^2)^{3/2}} . \quad (27)$$

Here, $\rho_{\text{gas}} = \mu n m_p$ represents the average gas density of the environment, given by the product of the average molecular weight $\mu = 1.22$, the gas number density n , and the proton mass m_p . Furthermore, c_s represents the sound speed determined by the gas temperature, and v_{rel} is the relative velocity of the BH with respect to the gas. Thus, the effective velocity is given by $v_{\text{eff}} = \sqrt{c_s^2 + v_{\text{rel}}^2}$. We also note that for binary BHs the accretion rate could be modified compared to single BHs with the same mass. However, the change in the magnitude of the accretion rate is still under debate, as some simulations identify suppressed accretion rates because of the gravitational torque exerted by binaries (e.g. MacFadyen & Milosavljević 2008; Miranda et al. 2017), whereas others find that binary accretion rates are not

significantly modified (e.g. Farris et al. 2014; Shi & Krolik 2015). Therefore, for simplicity, we assume a single BH accretion rate for all BHs.

Next, we introduce a dimensionless accretion factor:

$$\dot{m} \equiv \frac{\dot{M}_\bullet}{\dot{M}_{\text{Edd}}}, \quad (28)$$

where \dot{M}_{Edd} represents the Eddington accretion rate given by:

$$\dot{M}_{\text{Edd}} = 2.7 \times 10^{-7} M_\odot \text{yr}^{-1} \left(\frac{M_\bullet}{10 M_\odot} \right) \left(\frac{\epsilon_0}{0.1} \right)^{-1}. \quad (29)$$

Here, ϵ_0 refers to the radiative efficiency.

3.1 Black Holes in the IGM

Since there is no process that allows for star formation in the IGM, we here only consider the case of PBH accretion. For the convenience of the reader, we provide a brief summary of the relevant analytical formalism, as developed in previous studies. For PBH accretion in the IGM, we adopt the self-similar model that incorporates spherical Bondi accretion with the damping effect of Compton drag and Hubble flow at high redshifts (Ricotti 2007; Ricotti et al. 2008; Ali-Haïmoud & Kamionkowski 2017). For isolated PBH accretion in the IGM, the accretion factor, normalized to typical values, can be expressed as follows⁶:

$$\dot{m} = 3.40 \times 10^{-3} \lambda \left(\frac{1+z}{1000} \right)^3 \left(\frac{M_\bullet}{10 M_\odot} \right) \left(\frac{v_{\text{eff}}}{10 \text{ km s}^{-1}} \right)^{-3}. \quad (30)$$

Here, λ represents a scaling constant that represents the damping effect, numerically fitted as follows:

$$\lambda = \exp \left(\frac{9/2}{3 + \hat{\beta}^{0.75}} \right) \frac{-1 + (1 + \hat{\beta})^{1/2}}{\hat{\beta}}. \quad (31)$$

The effective viscosity $\hat{\beta}$ is in turn determined by the Compton drag and Hubble flow, given by:

$$\hat{\beta} = 4.4 \times 10^{-4} \left(\frac{M_\bullet}{10 M_\odot} \right) \left(\frac{1+z}{1000} \right)^{3/2} \left(\frac{v_{\text{eff}}}{10 \text{ km s}^{-1}} \right) \times \left[1 + 56.3 \left(\frac{x_e}{10^{-3}} \right) \left(\frac{1+z}{1000} \right)^{5/2} \right]. \quad (32)$$

Here, x_e represents the ionization fraction as a function of redshift. For simplicity, we approximate x_e as a step function, in line with the CMB constraint from Planck Collaboration et al. (2020). For $6 \leq z \leq 1000$, which extends to epochs long after recombination, we take its value to be a constant⁷, specifically $x_e \sim 10^{-3}$. For $z \leq 6$, after reionization, this factor is set to 1. In all cases considered, we have $\hat{\beta} \ll 1$. Then, the scaling constant can be approximated as $\lambda \simeq \exp(3/2)/2 \simeq 2.24$.

For the gas effective velocity v_{eff} in the IGM, we adopt the analytical approximation from Ricotti et al. (2008) and Ali-Haïmoud

& Kamionkowski (2017) by averaging over the Maxwell velocity distribution for PBHs:

$$\langle v_{\text{eff}} \rangle \sim c_s \left(\frac{16}{\sqrt{2\pi}} \mathcal{M}^3 \right)^{1/6} \theta(\mathcal{M} - 1) + c_s \left(1 + \mathcal{M}^2 \right)^{1/2} \theta(1 - \mathcal{M}). \quad (33)$$

Here, $\mathcal{M} = \langle v_{\text{rel}} \rangle / c_s$ represents the Mach number, and $\langle v_{\text{rel}} \rangle$ is the root-mean-square of the relative velocity between dark matter (DM) and baryons, approximated as⁸:

$$\langle v_{\text{rel}} \rangle \approx \min \left[1, z/10^3 \right] \times 30 \text{ km s}^{-1}. \quad (34)$$

The gas sound speed, c_s , is calculated from the CMB temperature, which is a function of redshift. We use the parametric fit given in De Luca et al. (2020b):

$$c_s \simeq 5.70 \left(\frac{1+z}{1000} \right)^{1/2} \left[\left(\frac{1+z_{\text{dec}}}{1+z} \right)^\beta + 1 \right]^{-1/2\beta} \text{ km s}^{-1}. \quad (35)$$

Here, $\beta = 1.72$ is a fitting parameter, and $z_{\text{dec}} \simeq 130$ the decoupling redshift for baryons from the radiation field. Combining Equ. (29) and (30), we can approximate the mass growth rate as:

$$\dot{M}_\bullet \sim 2.7 \times 10^{-7} \dot{m} \left(\frac{M_\bullet(t)}{10 M_\odot} \right) \left(\frac{\epsilon_0}{0.1} \right)^{-1} M_\odot \text{yr}^{-1}. \quad (36)$$

Using the above equations to calculate the accretion rate and integrating over cosmic time, we find that for PBH masses of interest, $M_{\text{PBH}} \lesssim 100 M_\odot$, the change in mass is $\delta M_{\text{PBH}} / M_{\text{PBH}} \ll 1$, which is negligible. Therefore, to make conservative estimates and simplify our calculations, for PBH accretion in the IGM, we assume a mass function $\psi(M)$ that is independent of redshift. However, we also note that, although yet to be observed, the accretion rate of PBHs, \dot{m} , could exceed the Eddington limit, if DM haloes are seeded by more massive PBHs (with $\gg 100 M_\odot$) in isolation (e.g. Ricotti 2007; Mack et al. 2007; Ricotti et al. 2008; De Luca et al. 2020a). In this scenario, the PBH can accrete a significant amount of mass by $z \lesssim 6$, thus significantly changing the shape of the PBH mass function. To fully address this effect, a dedicated simulation study would be required following up on the work by Liu & Bromm (2022b).

3.2 Black Holes in haloes

For the case of accretion within virialized haloes, we encounter more complexity compared to the previous case, since there will be BHs of various origins within a given DM halo. To simplify the calculations, we assume that both SRBHs and PBHs undergo Bondi accretion:

$$\dot{m} = 3.2 \times 10^{-6} \left(\frac{M_\bullet}{10 M_\odot} \right) \left(\frac{n(r)}{1 \text{ cm}^{-3}} \right) \left(\frac{\mu}{1.22} \right) \left(\frac{v_{\text{eff}}}{10 \text{ km/s}} \right)^{-3}. \quad (37)$$

Here, for a BH at a given radius r relative to the center of the halo, $n(r)$ is the local gas number density. For the case of monochromatic PBHs, we use the simulated results from Liu et al. (2022), suggesting a nearly isothermal gas density profile⁹: $n(r) \propto r^{-2.2}$. Additionally,

⁸ We use a slightly different prescription for $\langle v_{\text{rel}} \rangle$ vs. z , as compared to Ricotti et al. (2008), by considering the relative motion between DM and baryons in non-linear perturbation theory (see e.g. Tseliakhovich & Hirata 2010; Stacy et al. 2011; Dvorkin et al. 2014).

⁹ Here we assume that gas is always able to collapse into a quasi-isothermal sphere despite the feedback from accreting PBHs. However, collapse of gas may be delayed/halted by BH feedback in low-mass ($\lesssim 10^8 M_\odot$) haloes without atomic cooling, which can lead to shallower gas density profiles and lower BH accretion rates (Liu et al. 2024). The effects of local BH feedback on gas properties are still in debate. Our results based on the quasi-isothermal gas density profile should be regarded as optimistic estimates.

⁶ We will also consider the effect of enhanced accretion by DM clothing surrounding individual PBHs, since we here assume that PBHs do not comprise the entirety of DM. This is presented in Appendix C.

⁷ For the case of PBH accretion in the IGM, previous studies have calculated the ionization fraction, e.g. Ziparo et al. (2022). In their study, although x_e changes by an order of ~ 100 with respect to $f_{\text{PBH}} \sim 10^{-4} - 1$, this factor has a negligible effect on $\hat{\beta}$.

we assume the same scaling for the PBH number density. For SRBHs, we assume a similar density profile for simplicity, since the formation of SRBHs should approximately track the gas density profile, which in turn has a similar shape as the DM density profile in this regime, according to previous simulation results (see fig. 7 in Liu et al. 2022). Further simulation studies will be needed to more realistically track the location of SRBHs vs. PBHs in a halo, including any dynamical segregation effects at later stages. Meanwhile, we use the virial velocity as the effective velocity v_{eff} between BHs and the gas:

$$v_{\text{eff}} \sim \sqrt{\frac{GM_h}{R_{\text{vir}}}} \sim 5.4 \text{ km s}^{-1} \left(\frac{M_h}{10^6 M_\odot} \right)^{\frac{1}{3}} \left(\frac{1+z}{21} \right)^{-\frac{1}{2}}. \quad (38)$$

Here, R_{vir} is the virial radius of the halo, which is related to halo mass and redshift by:

$$R_{\text{vir}} \sim 0.147 \left(\frac{\Delta_c}{18\pi^2} \right)^{-1/3} \left(\frac{M_h}{10^6 M_\odot} \right)^{1/3} \left(\frac{1+z}{21} \right)^{-1} \text{ kpc}, \quad (39)$$

where Δ_c is the characteristic overdensity of the halo with respect to the cosmic average, and we adopt a fiducial value of 200. We note that for certain cases of BH accretion, Equ. (37) could yield rates larger than the Eddington limit. Conservatively, we enforce $\dot{m} \lesssim 1$ throughout, and thus do not consider any super-Eddington accretion regime, which we cannot reliably represent with our idealized modeling here.

The dynamics and density distribution of PBHs with an extended mass function can be complex, and its effect on SRBH and SMBH formation would require future simulations. Additionally, SRBHs will also have a non-trivial mass function, adding further complexity to the situation. For now, we can derive order of magnitude estimations. We assume that the extended PBH mass distribution will not significantly change the density profiles of both gas and BHs in the host halo. To calculate the gas number density at different radii, we normalize to the value at the virial radius:

$$\begin{aligned} n(R_{\text{vir}}) &\sim \Omega_b (1+z)^3 \frac{3H_0^2 \Delta_c}{8\pi G \mu m_p} \\ &\sim 0.33 \left(\frac{\Delta_c}{18\pi^2} \right) \left(\frac{\mu}{1.22} \right)^{-1} \left(\frac{1+z}{21} \right)^3 \text{ cm}^{-3}. \end{aligned} \quad (40)$$

Similarly, since no previous simulations have considered the evolution of PBHs and SRBHs, for simplicity, we apply the same formula to calculate the accretion rate for both BH classes. To further simplify our calculations, we impose additional assumptions, as follows. For more massive SRBHs (with progenitor stellar mass $\gtrsim 260 M_\odot$), we assume that they gradually sink towards the halo center to become seeds for SMBHs, or get captured by the pre-existing central SMBH. Thus, we cut off the progenitor stellar mass functions for SRBHs at $\gtrsim 260 M_\odot$ and restrict their radii to be inside of $0.001 R_{\text{vir}}$. Typically, for a $10^9 M_\odot$ halo at $z \simeq 10$, the virial radius is $R_{\text{vir}} \sim 3 \text{ kpc}$. The inner region, $r < 0.001 R_{\text{vir}}$, thus has a size $\sim \mathcal{O}(\text{pc})$, and can only contain a SMBH. For PBHs following a log-normal mass function, we numerically integrate from $0.1 - 10 M_c$ to cover the plausible mass range.

Furthermore, we assume a time independent mass function for both PBHs and SRBHs (excluding HMXBs). We find that any evolution of the BH mass function in a halo is likely small, as we argue below. Since the halo will also capture PBHs during its growth, we can compare the total PBH accretion rate with the capture rate of PBHs by DM halo accretion. A fiducial value for the capture rate is the accretion rate calculated for the Millennium simulation (McBride et al. 2009), modified for a contribution from PBH DM, as expressed

in the PBH mass fraction f_{PBH} :

$$\begin{aligned} \langle \dot{M}_{\text{PBH,tot}} \rangle &\sim 0.02 M_\odot \text{ yr}^{-1} \left(\frac{M_h}{10^{12} M_\odot} \right)^{1.094} \left(\frac{f_{\text{PBH}}}{10^{-3}} \right) \\ &\times (1 + 1.75z) \sqrt{\Omega_m (1+z)^3 + (1 - \Omega_m)}. \end{aligned} \quad (41)$$

This is of the same order of magnitude as the accretion rate obtained by integrating over all PBHs with a characteristic mass of $100 M_\odot$ in a $10^{12} M_h$ halo at $z = 0$, as given by Equ.(36)-(40). Therefore, at higher redshifts, we would expect a much larger PBH capture rate than the total accretion rate. For SRBHs, we find that the increase in total SRBH mass is proportional to the star formation rate, i.e. $\sim 0.01 \text{ SFH}(M_h, z)$, as calculated using Equ.(20), which is also significantly larger than the total accretion rate. In both cases, the newly increased BH population will likely preserve the mass function at formation. In general, however, the overall BH mass function in a given halo will result from the competition between the BHs that already sit in the halo versus newly accreted or born BHs. Although we do not explore such cases here, a more complete treatment should broaden the discussion. A more detailed simulation study of the mass function evolution within a DM halo would be necessary in future work. For now, we can accommodate only minor changes to the overall mass function of SRBHs and PBHs. Finally, for HMXBs and SMBHs, we note that feedback could affect the accretion efficiency in complex ways.¹⁰ For simplicity and consistent with the prescription in Jeon et al. (2014), we impose Eddington-limited accretion throughout ($\dot{m} = 1$).

4 RADIATIVE SIGNATURE

4.1 Cosmic Radiation Background

In this section, we aim to study the contribution from all BHs, as summarized in Figure 1, to the cosmic radiation background. Here, we focus on cases with monochromatic PBH mass distribution, and defer fully explored results for an extended mass distribution to future work. We begin by splitting the energy density u from BH feedback into two parts based on the BH habitat:

$$u = u_{\text{IGM}} + u_{\text{halo}}, \quad (42)$$

where u_{IGM} represents the energy feedback from PBHs accreting in the IGM, and u_{halo} that from all BHs in DM haloes. Based on the DM halo mass, we further decompose the feedback in collapsed structures into contributions from SRBHs (including HMXBs), PBHs, and SMBHs, as follows:

¹⁰ Feedback effects in SMBHs play a dual role, where kinetic-mode feedback self-regulates gas accretion, decreasing the Eddington ratios and limiting mass growth (see e.g. Weinberger et al. 2018), while super-Eddington accretion, in the absence of feedback, can significantly increase SMBH mass in a fraction of the Eddington time (e.g. Li 2012). In HMXBs, the accretion efficiency is significantly impacted by the presence of accretion disks, leading to super-Eddington rates in ultraluminous X-ray sources (ULXs), and modulated by interactions between stellar winds and the black hole's gravitational influence, as seen in systems like Cyg X-1 (for a review on HMXBs see Fornasini et al. 2023).

$$u_{\text{halo}} = \begin{cases} u_{\text{PBH}}, & (M_{\text{min}}(z) \leq M_{\text{h}} < M_{\text{H}_2\text{-cool}}) \\ u_{\text{SRBH}} + u_{\text{HMXB}} + u_{\text{PBH}}, & (M_{\text{H}_2\text{-cool}} \leq M_{\text{h}} < 10^8 M_{\odot}) \\ u_{\text{SRBH}} + u_{\text{HMXB}} + u_{\text{PBH}} + u_{\text{SMBH}}, & (10^8 M_{\odot} \leq M_{\text{h}} < M_{\text{max}}(z)) \end{cases} \quad (43)$$

Here, several DM halo mass limits are introduced. Specifically, $M_{\text{min}}(z)$ refers to the smallest halo mass that could host a PBH, given by $M_{\text{min}} = \max(M_c \Omega_m / f_{\text{PBH}} \Omega_{\text{DM}}, M_{\text{vir}})$, where M_{vir} refers to the smallest mass that can virialize at a given redshift into a halo structure with a virial temperature $\gtrsim 100$ K. We also notice some other pertinent mass scales, such as $\sim M_c(1 + z_{\text{eq}})/(1 + z)$, describing a halo seeded by a single PBH (see e.g. Ricotti 2007; Ricotti et al. 2008). This effect will further increase the radiation output since more minihaloes are present at high redshift. In our modeling, we derive a conservative estimate with the current choice of mass threshold and address the PBH-seeded halo case in Appendix C. We defer a more complete understanding of halo accretion at high redshifts to future study with simulations.

$M_{\text{H}_2\text{-cool}}$ is the smallest mass of a DM halo capable of forming Pop III stars via H_2 cooling, and it is fitted by $M_{\text{H}_2\text{-cool}} \approx 1.54 \times 10^5 M_{\odot} [(1 + z)/31]^{-2.074}$ (Trenti & Stiavelli 2009). $M_{\text{max}}(z)$ is the maximum allowed mass of DM haloes at redshift z , given by the progenitor of $\sim 10^{16} M_{\odot}$ haloes at $z = 0$, following their growth history¹¹. Haloes with mass larger than $M_{\text{max}}(z)$ are excluded due to low number density. The growth trajectories of all haloes are modeled by Behroozi et al. (2013) and Behroozi & Silk (2018) (see Appendix A). For PBHs in haloes, since this halo growth model might not be applicable at high redshift, we set a uniform upper limit of $10^{13} M_{\odot}$ for numeric approximation.

To calculate each term, we need to revisit the accretion physics and study the radiative efficiency based on the accretion rate. As a good estimation, we adopt the sub-grid model from Negri & Volonteri (2017) to capture the transition from a radiatively efficient thin disk to an optically thick and advection-dominated accretion flow (ADAF) case. The relationship between BH accretion rate \dot{m} and bolometric luminosity is given by:

$$L = \epsilon_{\text{EM}} \dot{M}_{\bullet} c^2, \quad \epsilon_{\text{EM}} = \frac{\epsilon_0 A \dot{m}}{1 + A \dot{m}}. \quad (44)$$

where ϵ_{EM} is the electromagnetic efficiency, $A = 100$, and $\epsilon_0 = 0.057$ the radiative efficiency for optically thin accretion. Note that ϵ_{EM} reduces to ϵ_0 for higher accretion rates, $\dot{m} \gg 0.01$.

To evaluate the total luminosity from BH accretion in a halo of mass M_{h} at redshift z , we sum over the mass distributions of BHs, and normalize with respect to the BH mass function. In a general form, the total luminosity from BHs of a single origin is given by:

$$L_{\bullet}(M_{\text{h}}, z) = \sum_i \Delta N_{\bullet,i}(M_{\bullet}, M_{\text{h}}) L(M_{\bullet}) \\ = M_{\bullet,\text{tot}}(M_{\text{h}}) \frac{\int_{M_{\bullet,\text{min}}}^{M_{\bullet,\text{max}}} \psi(M_{\bullet}) L(M_{\bullet}) dM_{\bullet}}{\int_{M_{\bullet,\text{min}}}^{M_{\bullet,\text{max}}} \psi(M_{\bullet}) M_{\bullet} dM_{\bullet}}, \quad (45)$$

where $\Delta N_{\bullet,i}(M_{\bullet}, M_{\text{h}})$ is the number of BHs in mass bin i of width

ΔM_{\bullet} , within a halo of mass M_{h} at redshift z . Furthermore, $L(M_{\bullet})$ is the luminosity associated with BHs of mass M_{\bullet} , and $\psi(M_{\bullet})$ is the BH mass distribution function in a general form. To obtain the total number of BHs, we divide the total BH mass in a halo, $M_{\bullet,\text{tot}}(M_{\text{h}})$, by the average BH mass, as calculated in the denominator of the second equality above. When integrating, $M_{\bullet,\text{min}}$ and $M_{\bullet,\text{max}}$ represent the respective BH mass limits. For PBHs, we substitute the denominator with the characteristic BH mass M_c , and integrate over the mass range of $0.1 - 10M_c$. For SRBHs and HMXBs, we employ Equ. (17-19) with the mass limits discussed in Section 2.3. For SMBHs, we assume that each massive halo contains one central SMBH, and that the luminosity is given by the Eddington value, $L_{\bullet} \approx L_{\text{Edd}}(M_{\bullet}) \approx \epsilon_0 \dot{M}_{\text{Edd}} c^2$.

Once we have the aggregate power from one type of BH in a halo of mass M_{h} at redshift z , the (proper) average power density, $j_{\bullet}(z)$, is obtained by integrating over the halo mass function, as mentioned previously:

$$j_{\bullet}(z) = \int_{M_{\text{min}}(z)}^{M_{\text{max}}(z)} (1+z)^3 n(M_{\text{h}}, z) L_{\bullet}(M_{\text{h}}, z) dM_{\text{h}}, \quad (46)$$

where $n(M_{\text{h}}, z)$ is the comoving number density of haloes per unit halo mass, given by Equ.(9). The factor of $(1+z)^3$ is applied to derive the physical number density at a given z . We note that, if the maximum halo mass M_{max} is smaller than the lower limit M_{min} at some redshift z , there is no contribution from that particular type of BH. The lower integration limit M_{min} depends on the BH type. For PBHs located in a halo, $M_{\text{min}} = \max(M_c \Omega_m / f_{\text{PBH}} \Omega_{\text{DM}}, M_{\text{vir}})$. For SRBHs, we choose $M_{\text{min}} = M_{\text{H}_2\text{-cool}}$, whereas for SMBHs, we adopt $M_{\text{min}} = 10^8 M_{\odot}$ as the minimum halo mass that can host an AGN. The proper bolometric power density u at redshift z from BHs can be obtained by integrating the power density at a given redshift z' from different sources over cosmic time:

$$u(z) = \int_{z_i}^z \left(\frac{1+z}{1+z'} \right)^4 j_{\bullet}(z') \left| \frac{dt}{dz'} \right| dz', \quad (47)$$

where z_i and z are the initial and final redshift of consideration, respectively. Here, we consider the most distant PBH source emitting at $z_i \approx 1000$. For the case of SRBHs, we start the integration from $z_i \approx 50$.

The results are shown in Figure 5 for different PBH mass fractions: $f_{\text{PBH}} = 10^{-3}$ (upper panel) and $f_{\text{PBH}} = 10^{-5}$ (lower panel), both assuming a monochromatic mass distribution with $M_c = 10 M_{\odot}$. The figure confirms our previous statement that PBHs can only make up a small fraction of dark matter, as otherwise reionization would have occurred too early (see below for further discussion). If we assume a PBH mass fraction of 10^{-3} , the feedback power from PBHs in haloes starts to dominate at $z \lesssim 30$. We also note that, since SMBHs and HMXBs are accreting at a much higher rate than SRBHs, their emission power at lower redshift ($z \lesssim 10$) starts to surpass that from SRBHs. In addition, we discuss the energy output from the enhanced accretion rate within PBH-seeded halos in Appendix C.

For context, we compare our predicted bolometric luminosities to the lower limits on the cosmic radiation density required for key cosmological signatures. To render the 21-cm hyperfine structure line of neutral hydrogen detectable in the form of absorption, its internal spin temperature needs to be coupled to the IGM kinetic temperature. An effective way to accomplish this coupling is through the Wouthuysen-Field effect (Wouthuysen 1952; Field 1959), where Lyman- α photons scatter with H atoms, thus indirectly modifying the hyperfine level populations (Madau et al. 1997). We can estimate the required Lyman- α energy density, in proper units and assuming a flat spectrum, as follows: $u_{\text{Ly}\alpha} \approx 4\pi J_{\alpha} \nu_{\alpha} / c \gtrsim$

¹¹ For a typical value, $M_{\text{max}} \lesssim 10^{13} M_{\odot}$ at redshift 6.

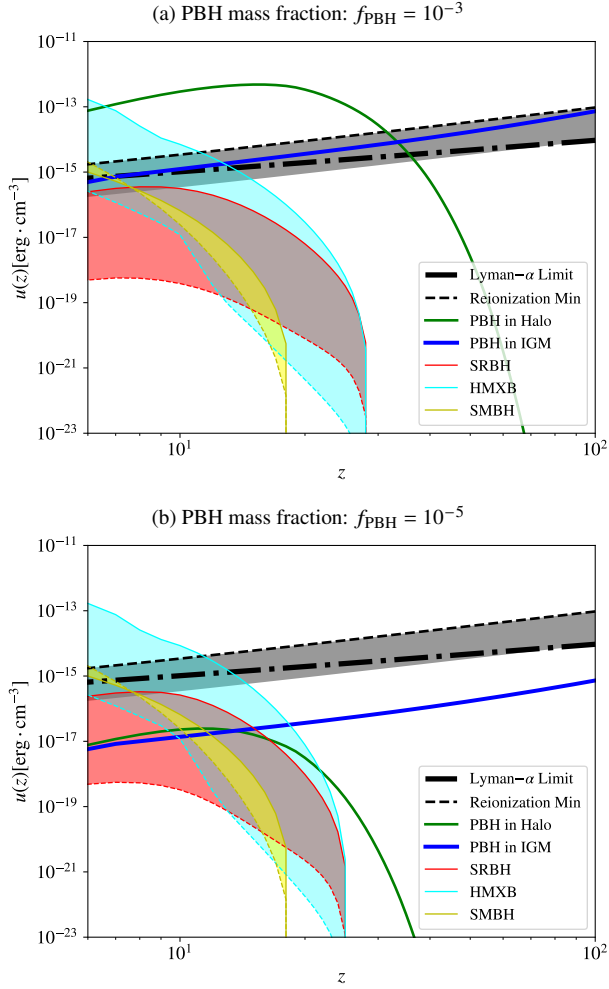


Figure 5. Integrated (bolometric) energy density from BH accretion feedback of different origins vs. redshift: PBHs in the IGM (blue), in haloes (green), SRBHs (red), HMXBs (cyan), and SMBHs (yellow). For PBHs, we assume a monochromatic mass distribution with $M_c = 10 M_\odot$, and mass fractions of $f_{\text{PBH}} = 10^{-3}$ (upper panel) and 10^{-5} (lower panel). Here, we consider the same range for the abundance of BHs as shown in Figure 4, when deriving possible radiation outputs. For comparison, we also plot the minimum Lyman- α flux required for Wouthuysen-Field coupling (dot-dashed line; from Ciardi & Madau 2003), as well as the minimum UV flux required for reionization (dashed line and grey-shaded area; from Madau et al. 1999).

$3.5 \times 10^{-14} [(1+z)/7]$ erg cm $^{-3}$ (Ciardi & Madau 2003). Similarly, we can estimate the minimum energy density in H-ionizing UV radiation required to reionize the IGM: $u_{\text{UV}} \simeq 4\pi J_{\text{UV}} \nu_{\text{UV}} / c \gtrsim 2 \times 10^{-15} [(1+z)/7]^{1.5}$ erg cm $^{-3}$ (Madau et al. 1999). However, to gauge the possible impact of PBH DM on cosmic reionization, we need to go beyond bolometric quantities, towards a more careful spectral modelling for accreting BHs (see below). Furthermore, any reionization constraints have to take into account the escape fraction of UV radiation from the source host haloes.

To obtain the (angle-averaged) radiation intensity at frequency ν and a given redshift z , we need to calculate the specific emission coefficient, $j_{\bullet, \nu'}(z')$, from sources at higher redshifts $z' > z$ with $\nu' = \nu(1+z)/(1+z')$. Applying the same procedure as for Equ. (45-46) but replacing the bolometric luminosity with the specific luminosity, i.e. $L \rightarrow L_\nu$ (per BH), $L_\bullet \rightarrow L_{\bullet, \nu}$ (per halo), and $j_\bullet \rightarrow j_{\bullet, \nu}$, we first sum over the contributions from all BHs in a halo, and

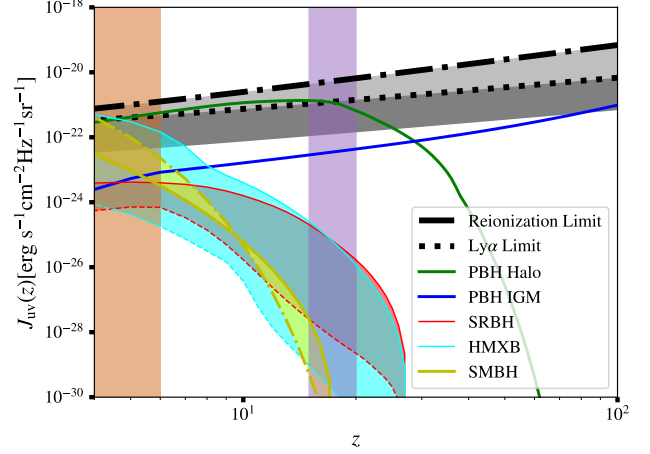


Figure 6. Background intensity at the Lyman limit, $\nu_{\text{UV}} = 13.6 \text{ eV}/h$, vs. redshift. Here, we again consider various BH sources (PBHs, SRBHs, HMXBs, and SMBHs), differentiating between halo and IGM PBH contributions. For the sake of simplicity, we assume a monochromatic mass function for PBHs with a characteristic mass of $10 M_\odot$ and a mass fraction of 10^{-3} . We show the minimum intensity, J_{UV} , required for reionization (Madau et al. 1999), as well as the minimum Lyman- α background, J_α , needed for efficient Wouthuysen-Field (WF) coupling (Ciardi & Madau 2003). For the comparison to the latter, we for simplicity assume $\nu_\alpha \simeq \nu_{\text{UV}}$, and for both limits, we indicate uncertainties with a factor-of-ten range (grey shaded areas). We also indicate the timing constraint for effective WF coupling at $z \sim 15 - 20$ (purple shaded area), inferred from the EDGES 21cm-cosmology measurement (Mirocha & Furlanetto 2019). Additionally, the brown region denotes the reionization limit at $z \sim 6$.

then integrate the halo mass function to obtain the specific emission coefficient. Here, the features of the emerging spectrum from a single BH depend mostly on the normalized accretion rate \dot{m} , determining whether accretion operates in the thin-disk or ADAF regime. We employ the prescription of Takhistov et al. (2022), as summarized in Appendix B, to calculate the specific luminosity $L_\nu(M_\bullet)$ for any BH. Finally, integrating all contributions from preceding redshifts, the resulting specific intensity J_ν at z is (e.g. Schauer et al. 2019):

$$J_\nu(z) = \frac{c}{4\pi} \int_{z_i}^z \left(\frac{1+z}{1+z'} \right)^3 j_{\bullet, \nu'}(z') \left| \frac{dt}{dz'} \right| dz'. \quad (48)$$

We note that both Equ. (47) and (48) have no absorption term, thus assuming a transparent IGM and maximizing the radiation level from BH sources. Therefore, z_i denotes the largest redshift that a given BH source starts to emit light. To calculate the intensity for a given frequency band, we simply integrate J_ν over the corresponding band, and z_i denotes the highest redshift below which radiation produced by BHs can reach z in the given band. In the following sub-sections, we will specifically discuss the intensity in the UV and X-ray bands, comparing them with observational constraints. We emphasize that when evaluating the resulting feedback on the IGM, the escape fraction f_{esc} of radiation from the host haloes should be taken into account, depending on the waveband considered. For now, and unless otherwise noted, we set the escape fraction to 1, thus maximizing the radiative output from the accreting BH sources (further discussed below).

4.2 UV Intensity

In Figure 6, we present our calculations of the (average) UV intensity from BHs as a function of redshift, assuming a monochromatic mass function for PBHs with a characteristic mass $M_c = 10 M_\odot$ and a mass fraction $f_{\text{PBH}} = 10^{-3}$. We evaluate the radiation intensity at $\nu_{\text{UV}} = 13.6 \text{ eV}/h$, and assume for simplicity the same value at ν_α , i.e. $J_\alpha \approx J_{\text{UV}}$, which is sufficiently precise for our purpose here. It is evident that while the contribution from PBHs in the IGM initially dominates, it becomes significantly smaller compared to the radiation from BHs in haloes for $z \lesssim 30$. Our estimation of the UV power from SMBHs is about an order of magnitude lower than the findings in Jeon et al. (2022). This discrepancy arises because of differences in the spectral modeling, employing a more detailed approach here (see Appendix B). Another contributing factor might be our model's prediction of a BH mass that is smaller by roughly a factor of ~ 10 when compared to observed high-redshift quasars (e.g. Decarli et al. 2018; Wang et al. 2021).

According to a confluence of observations, the IGM was fully reionized by $z \sim 6$ (reviewed in Robertson et al. 2010), with early evidence based on the Gunn-Peterson absorption trough in high- z quasar spectra (e.g. Becker et al. 2001). When juxtaposing the reionization limit with the radiation background from all BHs, it is clear that PBHs consistently dominate over other BH sources prior to reionization, as long as $f_{\text{PBH}} \gtrsim 10^{-3}$. For our fiducial value of cosmic PBH density (0.1% of all DM), we can see that at $z \lesssim 15$, the UV intensity from PBHs (within haloes) becomes comparable to the level required for reionization, suggesting that they could be a significant source of ionizing photons for the neutral hydrogen in the IGM. Taken at face value, such large UV intensities would allow for reionization much earlier than the canonical redshift of $z \sim 6$. However, when calculating the resulting UV intensity, we have assumed that all ionizing photons produced via BH accretion inside a halo can escape from the host ($f_{\text{esc}} = 1$). More realistic treatments, despite the inherent uncertainty, have constrained this factor to be significantly smaller, around 0.1 for typical host systems in the pre-reionization Universe (e.g. Gnedin et al. 2008; Khaire et al. 2016). Given our ballpark calculations, as presented in Figure 6, PBH DM could contribute significantly to the sources of reionization. Depending on the (uncertain) UV escape fraction, this yields another constraint on the PBH DM fraction, roughly giving $f_{\text{PBH}} \lesssim 10^{-3}/f_{\text{esc}}$.

Similarly, we assess whether the PBH contribution to the cosmic Lyman- α background can induce Wouthuysen–Field coupling, thus imprinting a global absorption signature in the redshifted 21-cm radiation (e.g. Pritchard & Loeb 2012). Such a signature was reported by the Experiment to Detect the Global Epoch of Reionization Signature (EDGES), suggesting that the spin temperature of neutral hydrogen was coupled via the Wouthuysen-Field effect to the kinetic gas temperature around $z \simeq 15 - 20$ (Bowman et al. 2018; Mirocha & Furlanetto 2019). This claimed detection remains a topic of vigorous debate, with more recent spectral radiometer measurements that have found no such signal (Singh et al. 2022). Prior research (Mena et al. 2019) modeled the alterations in the kinetic temperature of IGM gas due to PBH heating, constraining the PBH abundance to $f_{\text{PBH}} \lesssim 10^{-3}$ for $M_c = 10 M_\odot$. Using the same characteristic mass, we find a similar constraint on the PBH abundance, as $f_{\text{PBH}} > 10^{-3}$ would imply effective Wouthuysen-Field coupling at redshifts larger than the EDGES range (see Fig. 6). We note that in arriving at this conclusion, we have assumed an escape fraction for Lyman- α photons of close to unity, which is plausible for the dust-poor galaxies at cosmic dawn (e.g. Jaacks et al. 2018; Smith et al. 2019). As our results indicate, accreting PBHs located within haloes are possibly

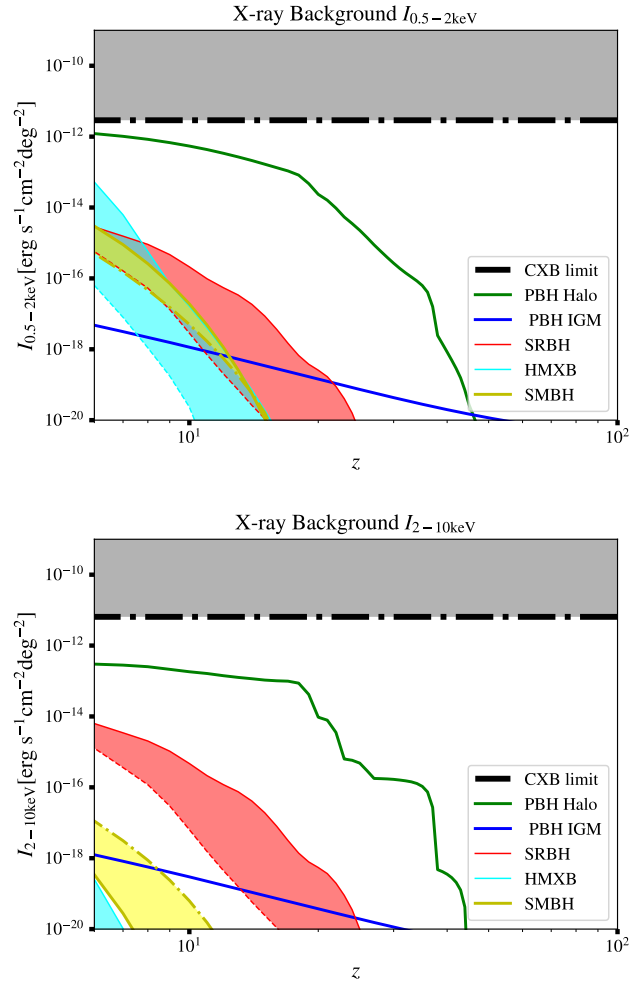


Figure 7. Contribution of accreting high- z BH sources to the present-day ($z = 0$) X-ray background. X-ray intensities are plotted against redshift for all BH sources considered here, applying the same set of parameters as used in Figure 6. The black dash-dotted line represents the unresolved X-ray background (Cappelluti et al. 2017, 2022). The upper panel shows the soft X-ray band with a photon energy in the $[0.5 - 2\text{keV}]$ range, while the lower panel depicts the integrated hard X-ray band with photon energies of $[2 - 10\text{keV}]$.

potent sources for Lyman- α background radiation at high redshifts, whereas the other BH sources considered here fall short in producing a significant number of Lyman- α photons. For a discussion of the contribution of stellar sources to the cosmic Lyman- α radiation field, we refer to the extensive literature on this topic (e.g. Fialkov & Barkana 2014; Schauer et al. 2019; Gessey-Jones et al. 2022).

4.3 X-ray Intensity

In Figure 7, we illustrate the contribution of BHs from various sources to the unresolved portions of the present-day hard ($[2 - 10 \text{ keV}]$) and soft ($[0.5 - 2 \text{ keV}]$) X-ray backgrounds, again considering PBHs with $M_c = 10 M_\odot$ for a monochromatic mass function and $f_{\text{PBH}} = 10^{-3}$. The X-ray background intensity in a given energy band $[E_1 - E_2]$ is $I_{E_1-E_2} = \int_{\nu_1}^{\nu_2} J_\nu d\nu$, $\nu_i = E_i/h$, $i = 1, 2$, where h is the Planck constant. We emphasize that any unresolved sources are preferentially expected at $z \gtrsim 6$, given the low luminosity of typical high-redshift

systems. It is thus natural to consider accreting BHs at cosmic dawn when accounting for the unresolved CXB. Note that when assessing the contribution of sources at z' to the radiation observed at $z = 0$, we use $\nu' = (1 + z')\nu$ for the integration involved in Equ. (48).

Our results for PBHs agree with the findings of Ziparo et al. (2022), when using identical parameter choices. However, by incorporating the effects of DM-baryon streaming and Compton drag, which diminish the accretion rate, we determine that PBHs in the IGM contribute only a minuscule fraction to the overall X-ray radiation. For $z \lesssim 30$, the BH feedback power from haloes becomes dominant, similar to the behaviour in the (rest-frame) UV band. Comparing our predicted radiation levels to the unresolved CXB inferred from deep Chandra observations (Cappelluti et al. 2017, 2022), we conclude that the accretion feedback from PBHs, located within haloes, may account for a substantial part of the missing X-ray flux. More specifically, in the soft X-ray band ([0.5 – 2 keV]), radiation from PBHs at $z \gtrsim 6$ almost reaches the intensity level of the unresolved X-ray background, whereas in the hard X-ray band ([2 – 10 keV]), radiation from these PBHs approaches the unresolved background intensity, but falls somewhat short. In both bands, the radiation from PBHs dominate over all other BH sources by at least an order of magnitude.

We note that neutral H and He in the IGM absorb soft X-ray photons ([0.5 – 2 keV]) more efficiently than hard X-ray radiation ([2 – 10 keV]), due to the approximately ν^{-3} dependence of the photo-ionization cross sections (e.g. Wilms et al. 2000). As a result, the upper panel in Figure 7 represents the upper limit for the soft X-ray contribution from PBHs. In summary, our calculations suggest that radiation from accreting PBHs at high redshifts may play a significant role in accounting for the unresolved portion of the cosmic X-ray background, given a PBH abundance parameter of $f_{\text{PBH}} \gtrsim 10^{-3}$.

5 SUMMARY AND CONCLUSIONS

We have investigated the impact of PBHs as a dark matter component on structure formation and radiation backgrounds in the early Universe. Taking into account the presence of PBHs, we have analyzed the energy feedback resulting from the accretion of matter by all BHs of various origins across cosmic history. Our study has led us to the following key findings and conclusions:

(i) From the constructed PBH- Λ CDM Universe, we find that even in the absence of initial clustering of PBHs, their presence will accelerate the formation of virialized structures (haloes), as the Universe becomes clumpy with the emergence of minihaloes of mass $\lesssim 10^6 M_{\odot}$. Increasing both PBH mass abundance and characteristic mass parameters will accelerate structure formation, with the former being more significant, as shown in Figure 2.

(ii) In the IGM, only PBHs are present. However, within DM haloes, we need to consider BHs formed through astrophysical channels in addition to PBHs. As the first stars begin to form, the remnants of these massive stars give rise to SRBHs. However, even assuming that PBHs constitute only a small fraction of the DM ($f_{\text{PBH}} \lesssim 10^{-3}$), we find that HMXBs and SMBHs start to generate comparable accretion power as PBHs within halo environments only at lower redshifts $z \lesssim 7$ (see Figs. 4 and 5).

(iii) Considering the evolving bolometric radiation energy density produced by BH accretion, we have observed that the power density from PBH accretion in DM haloes begins to dominate over that from accretion in the IGM at $z \lesssim 30$. Initially, the radiative output from PBHs dominates, but it becomes comparable to that from SRBHs around $z \sim 7$. However, if the PBH abundance were much greater

than $f_{\text{PBH}} \sim 10^{-3}/f_{\text{esc}}$, as shown in Figs. 5 and 6, the Universe would undergo reionization too early, in violation of existing constraints. This further supports the conclusion that PBHs within the solar mass range cannot be the primary component of dark matter.

(iv) We have found that by changing the mass function of PBHs from a monochromatic distribution to a log-normal one, there is a minor change in the total energy density, by a factor of approximately 2. Moreover, with a larger mass dispersion parameter σ , the overall energy density further increases. This can be explained by the fact that the scaling of the accretion power L with respect to BH mass is non-linear with a power-law index > 2 , as shown in Equ. (28–29), (37) and (44). However, since the combination of characteristic mass and PBH abundance parameters is highly constrained by Kühnel & Freese (2017), any effect from changing the mass function from monochromatic to log-normal is likely small.

(v) By modeling the spectral energy distribution (SED) of BH accretion feedback (see Appendix B), we can calculate the energy feedback at specific frequencies (bands). From Figure 6, we conclude that accretion onto PBHs could be an important source for generating sufficient UV and Lyman- α background radiation to affect cosmic reionization or to produce detectable absorption in the (redshifted) 21-cm line via efficient Wouthuysen-Field coupling. However, for $f_{\text{PBH}} \lesssim 10^{-3}$, no existing constraints would be violated. On the other hand, when comparing the X-ray power from accreting BHs with the limits on the unresolved X-ray background, as shown in Figure 7, we find that the total power from BH sources in DM haloes is comparable to the present-day unresolved X-ray background limit. Again, the accretion power from PBHs in the IGM is negligible. For PBHs within haloes, the X-ray power generated is always dominant over that by other BHs, in both soft and hard X-ray bands, with the difference in the latter being even stronger. The PBH contribution may thus reach the intensity level of the unresolved soft X-ray background, but falls somewhat short of the level of the hard X-ray background, for plausible values of f_{PBH} . We note that any conclusions for the soft X-ray background depend on the uncertain modeling of the optical depth to photo-ionization in the neutral IGM.

We would like to acknowledge several limitations in our study. Firstly, concerning the mass function of PBHs, we note that the predicted accretion rates in the IGM and virialized halos are negligibly small (see Equ. 37), rendering the mass function effectively time independent, within the characteristic mass range of $M_c \sim 1 - 100 M_{\odot}$. Previous studies (e.g., Hasinger 2020; De Luca et al. 2020a; Yuan et al. 2023) have attempted to address this issue using a semi-analytical approach with accretion models from Mack et al. (2007); Ricotti et al. (2008), where the accretion rate could be significantly enhanced within haloes seeded by PBHs in the IGM environment. We note that in the case of extended or monochromatic PBH mass functions with a large characteristic mass $M_c \gg 10 M_{\odot}$, the time-independent assumption will likely no longer be a good approximation. For PBHs in a virialized halo environment, changes to the mass function become more complex. Here, additional factors need to be considered, such as the distribution within haloes of PBHs with an extended mass function, the case of infalling PBHs through halo accretion from the cosmic web or through mergers with other haloes, and the merger of PBHs with other BHs. Selected recent studies have considered the possibility that BH binaries or massive BH seeds could form through PBH captures and mergers (see e.g. Hayasaki et al. 2016; Ali-Haïmoud et al. 2017; De Luca et al. 2020b, 2023). In this work, for the sake of simplicity, we ignored the effect of gravitational capture or merger, and assumed a time-independent PBH mass function, for both IGM and halo environments throughout cos-

mic history. Therefore, a more accurate modeling of the change in the mass function can be achieved through cosmological simulations, which we leave as a topic for future studies.

Any predictions for the radiation feedback from all BHs are subject to the broader uncertainties in modeling BH number densities and halo gas density profile (see footnote 9). As an example, not all galaxies will host a central SMBH, giving rise to AGN feedback. Furthermore, for HMXBs we may have overestimated the accretion rate and its duty cycle. Additionally, we have not considered the scattering/absorption attenuation caused by hydrogen and helium atoms due to the challenges in calculating source distributions. However, taking this additional factor into account would not significantly alter our main conclusions since it equally applies to BHs in haloes. Overall, we can still conclude that distinguishing PBHs from other BHs solely based on the cosmic radiation background is challenging.

In future work, we plan to test the robustness of our modeling, such as how halo density profiles may be modified in the presence of BHs, with cosmological simulations. Additionally, we will consider the PBH-generated emissions in other bands, in particular the near-infrared and radio bands. Such studies will serve to provide a more complete interpretation for ongoing or upcoming sky surveys, such as with Euclid (Amendola et al. 2018) or the Square Kilometre Array (SKA) (Weltman et al. 2020), to detect the imprints left on the early IGM by the presence of PBH dark matter.

ACKNOWLEDGEMENTS

BL is supported by the Royal Society University Research Fellowship.

DATA AVAILABILITY

The data and codes used in this article will be shared upon reasonable request to the corresponding authors.

REFERENCES

- Abbott B. P., et al., 2016, *Phys. Rev. Lett.*, 116, 061102
 Abbott R., et al., 2020, *Phys. Rev. Lett.*, 125, 101102
 Abbott R., et al., 2021, *ApJ*, 913, L7
 Acuña J. T., Tseng P.-Y., 2023, *Journal of High Energy Physics*, 2023, 117
 Afshordi N., McDonald P., Spergel D. N., 2003, *ApJ*, 594, L71
 Agazie G., et al., 2023, *ApJ*, 951, L8
 Ali-Haïmoud Y., Kamionkowski M., 2017, *Phys. Rev. D*, 95, 043534
 Ali-Haïmoud Y., Kovetz E. D., Kamionkowski M., 2017, *Phys. Rev. D*, 96, 123523
 Amendola L., et al., 2018, *Living Reviews in Relativity*, 21, 2
 Atrio-Barandela F., 2022, *ApJ*, 939, 69
 Bagui E., Clesse S., 2022, *Physics of the Dark Universe*, 38, 101115
 Becker R. H., et al., 2001, *AJ*, 122, 2850
 Behroozi P., Silk J., 2018, *MNRAS*, 477, 5382
 Behroozi P. S., Wechsler R. H., Conroy C., 2013, *ApJ*, 770, 57
 Behroozi P., Wechsler R. H., Hearin A. P., Conroy C., 2019, *MNRAS*, 488, 3143
 Behroozi P., et al., 2020, *MNRAS*, 499, 5702
 Bertone G., Cumberbatch D., Ruiz de Austri R., Trotta R., 2012, *J. Cosmology Astropart. Phys.*, 2012, 004
 Bird S., Cholis I., Muñoz J. B., Ali-Haïmoud Y., Kamionkowski M., Kovetz E. D., Raccanelli A., Riess A. G., 2016, *Phys. Rev. Lett.*, 116, 201301
 Bondi H., 1952, *MNRAS*, 112, 195
 Bowman J. D., Rogers A. E. E., Monsalve R. A., Mozdzen T. J., Mahesh N., 2018, *Nature*, 555, 67
 Boylan-Kolchin M., 2023, *Nature Astronomy*, 7, 731
 Cappelluti N., et al., 2017, *ApJ*, 837, 19
 Cappelluti N., Hasinger G., Natarajan P., 2022, *ApJ*, 926, 205
 Carr B. J., 1975, *ApJ*, 201, 1
 Carr B., Kühnel F., 2020, *Annual Review of Nuclear and Particle Science*, 70, 355
 Carr B., Silk J., 2018, *MNRAS*, 478, 3756
 Carr B., Kohri K., Sendouda Y., Yokoyama J., 2021, *Reports on Progress in Physics*, 84, 116902
 Chabrier G., 2003, *PASP*, 115, 763
 Chisholm J. R., 2006, *Phys. Rev. D*, 73, 083504
 Choptuik M. W., 1993, *Phys. Rev. Lett.*, 70, 9
 Ciardi B., Madau P., 2003, *ApJ*, 596, 1
 Clark J. S., Lohr M. E., Najarro F., Patrick L. R., Ritchie B. W., 2023, *MNRAS*,
 Clesse S., García-Bellido J., 2017, *Physics of the Dark Universe*, 15, 142
 De Luca V., Franciolini G., Pani P., Riotto A., 2020a, *Phys. Rev. D*, 102, 043505
 De Luca V., Franciolini G., Pani P., Riotto A., 2020b, *J. Cosmology Astropart. Phys.*, 2020, 052
 De Luca V., Franciolini G., Pani P., Riotto A., 2020c, *J. Cosmology Astropart. Phys.*, 2020, 044
 De Luca V., Desjacques V., Franciolini G., Riotto A., 2020d, *J. Cosmology Astropart. Phys.*, 2020, 028
 De Luca V., Franciolini G., Riotto A., Veermäe H., 2022a, *Phys. Rev. Lett.*, 129, 191302
 De Luca V., Franciolini G., Kehagias A., Pani P., Riotto A., 2022b, *Physics Letters B*, 832, 137265
 De Luca V., Franciolini G., Riotto A., 2023, *Phys. Rev. Lett.*, 130, 171401
 Decarli R., et al., 2018, *ApJ*, 854, 97
 Desjacques V., Riotto A., 2018, *Phys. Rev. D*, 98, 123533
 Diemer B., 2018, *ApJS*, 239, 35
 Dizgah A. M., Franciolini G., Riotto A., 2019, *Journal of Cosmology and Astroparticle Physics*, 2019, 001
 Dolgov A., Silk J., 1993, *Phys. Rev. D*, 47, 4244
 Dvorkin C., Blum K., Kamionkowski M., 2014, *Phys. Rev. D*, 89, 023519
 Escrivà A., Bagui E., Clesse S., 2023, *J. Cosmology Astropart. Phys.*, 2023, 004
 Farris B. D., Duffell P., MacFadyen A. I., Haiman Z., 2014, *ApJ*, 783, 134
 Feng J. L., 2010, *ARA&A*, 48, 495
 Fialkov A., Barkana R., 2014, *MNRAS*, 445, 213
 Field G. B., 1959, *ApJ*, 129, 536
 Finkelstein S. L., et al., 2022, *ApJ*, 940, L55
 Fornasini F. M., Antoniou V., Dubus G., 2023, arXiv e-prints, p. arXiv:2308.02645
 Fragos T., et al., 2013a, *ApJ*, 764, 41
 Fragos T., Lehmer B. D., Naoz S., Zezas A., Basu-Zych A., 2013b, *ApJ*, 776, L31
 Furtak L. J., et al., 2023, arXiv e-prints, p. arXiv:2308.05735
 Gessey-Jones T., et al., 2022, *MNRAS*, 516, 841
 Gnedin N. Y., Kravtsov A. V., Chen H.-W., 2008, *ApJ*, 672, 765
 Gouttenoire Y., Trifinopoulos S., Valogiannis G., Vanvlasselaer M., 2023, arXiv e-prints, p. arXiv:2307.01457
 Greene J. E., et al., 2024, *ApJ*, 964, 39
 Harikane Y., et al., 2022, *ApJS*, 259, 20
 Harikane Y., et al., 2023a, *ApJS*, 265, 5
 Harikane Y., et al., 2023b, *ApJ*, 959, 39
 Hasinger G., 2020, *J. Cosmology Astropart. Phys.*, 2020, 022
 Hawking S., 1971, *Monthly Notices of the Royal Astronomical Society*, 152, 75
 Hayasaki K., Takahashi K., Sendouda Y., Nagataki S., 2016, *PASJ*, 68, 66
 Heger A., Fryer C. L., Woosley S. E., Langer N., Hartmann D. H., 2003, *ApJ*, 591, 288
 Helgason K., Ricotti M., Kashlinsky A., Bromm V., 2016, *MNRAS*, 455, 282
 Husain R., Liu B., Bromm V., 2021, *MNRAS*, 508, 2169
 Inayoshi K., Visbal E., Haiman Z., 2020, *ARA&A*, 58, 27
 Inman D., Ali-Haïmoud Y., 2019, *Phys. Rev. D*, 100, 083528
 Inoue Y., Kusenko A., 2017, *J. Cosmology Astropart. Phys.*, 2017, 034

- Jaacks J., Finkelstein S. L., Bromm V., 2018, *MNRAS*, **475**, 3883
 Jeon M., Pawlik A. H., Bromm V., Milosavljević M., 2014, *MNRAS*, **440**, 3778
 Jeon J., Bromm V., Finkelstein S. L., 2022, *MNRAS*, **515**, 5568
 Kashlinsky A., 2016, *ApJ*, **823**, L25
 Kashlinsky A., 2021, *Phys. Rev. Lett.*, **126**, 011101
 Kashlinsky A., Mather J. C., Helgason K., Arendt R. G., Bromm V., Moseley S. H., 2015, *ApJ*, **804**, 99
 Kashlinsky A., Arendt R. G., Atrio-Barandela F., Cappelluti N., Ferrara A., Hasinger G., 2018, *Reviews of Modern Physics*, **90**, 025006
 Khaire V., Srikanth R., Choudhury T. R., Gaikwad P., 2016, *MNRAS*, **457**, 4051
 Klessen R. S., Glover S. C. O., 2023, *ARA&A*, **61**, 65
 Kocevski D. D., et al., 2023, *ApJ*, **954**, L4
 Kühnel F., Freese K., 2017, *Phys. Rev. D*, **95**, 083508
 Labbé I., et al., 2023, *Nature*, **616**, 266
 Larson R. L., et al., 2023, *ApJ*, **953**, L29
 Li L.-X., 2012, *MNRAS*, **424**, 1461
 Liu B., Bromm V., 2020a, *MNRAS*, **497**, 2839
 Liu B., Bromm V., 2020b, *ApJ*, **903**, L40
 Liu B., Bromm V., 2022a, *ApJ*, **937**, L30
 Liu B., Bromm V., 2022b, *ApJ*, **937**, L30
 Liu B., Meynet G., Bromm V., 2021, *MNRAS*, **501**, 643
 Liu B., Zhang S., Bromm V., 2022, *MNRAS*, **514**, 2376
 Liu B., Sartorio N. S., Izzard R. G., Fialkov A., 2024, *MNRAS*, **527**, 5023
 MacFadyen A. I., Milosavljević M., 2008, *ApJ*, **672**, 83
 Mack K. J., Ostriker J. P., Ricotti M., 2007, *ApJ*, **665**, 1277
 Madau P., Dickinson M., 2014, *ARA&A*, **52**, 415
 Madau P., Meiksin A., Rees M. J., 1999, *ApJ*, **475**, 429
 Madau P., Haardt F., Rees M. J., 1999, *ApJ*, **514**, 648
 Maiolino R., et al., 2023, *arXiv e-prints*, p. arXiv:2308.01230
 Matthee J., et al., 2023, *arXiv e-prints*, p. arXiv:2306.05448
 McBride J., Fakhouri O., Ma C.-P., 2009, *MNRAS*, **398**, 1858
 Mena O., Palomares-Ruiz S., Villanueva-Domingo P., Witte S. J., 2019, *Phys. Rev. D*, **100**, 043540
 Meszaros P., 1974, *A&A*, **37**, 225
 Mirabel I. F., Dijkstra M., Laurent P., Loeb A., Pritchard J. R., 2011, *A&A*, **528**, A149
 Miranda R., Muñoz D. J., Lai D., 2017, *MNRAS*, **466**, 1170
 Mirocha J., Furlanetto S. R., 2019, *MNRAS*, **483**, 1980
 Mo H., van den Bosch F. C., White S., 2010, *Galaxy Formation and Evolution*
 Narayan R., Yi I., 1995, *ApJ*, **452**, 710
 Natarajan P., Pacucci F., Ferrara A., Agarwal B., Ricarte A., Zackrisson E., Cappelluti N., 2017, *ApJ*, **838**, 117
 Negri A., Volonteri M., 2017, *MNRAS*, **467**, 3475
 Planck Collaboration et al., 2020, *A&A*, **641**, A6
 Poulin V., Serpico P. D., Calore F., Clesse S., Kohri K., 2017, *Phys. Rev. D*, **96**, 083524
 Power C., Wynn G. A., Combet C., Wilkinson M. I., 2009, *Monthly Notices of the Royal Astronomical Society*, **395**, 1146
 Press W. H., Schechter P., 1974, *ApJ*, **187**, 425
 Pringle J. E., 1981, *ARA&A*, **19**, 137
 Pritchard J. R., Loeb A., 2012, *Reports on Progress in Physics*, **75**, 086901
 Ricotti M., 2007, *ApJ*, **662**, 53
 Ricotti M., Ostriker J. P., Mack K. J., 2008, *ApJ*, **680**, 829
 Robertson B. E., Ellis R. S., Dunlop J. S., McLure R. J., Stark D. P., 2010, *Nature*, **468**, 49
 Salpeter E. E., 1955, *ApJ*, **121**, 161
 Sana H., et al., 2013, *A&A*, **550**, A107
 Sartorio N. S., et al., 2023, *MNRAS*,
 Schauer A. T. P., Liu B., Bromm V., 2019, *ApJ*, **877**, L5
 Serpico P. D., Poulin V., Inman D., Kohri K., 2020, *Physical Review Research*, **2**, 023204
 Shi J.-M., Krolik J. H., 2015, *The Astrophysical Journal*, **807**, 131
 Sidoli L., Paizis A., 2018, *MNRAS*, **481**, 2779
 Singh S., et al., 2022, *Nature Astronomy*, **6**, 607
 Smith A., Bromm V., 2019, *Contemporary Physics*, **60**, 111
 Smith A., Ma X., Bromm V., Finkelstein S. L., Hopkins P. F., Faucher-Giguère C.-A., Kereš D., 2019, *MNRAS*, **484**, 39
 Stacy A., Bromm V., 2013, *MNRAS*, **433**, 1094
 Stacy A., Bromm V., Loeb A., 2011, *ApJ*, **730**, L1
 Sureda J., Magaña J., Araya I. J., Padilla N. D., 2021, *MNRAS*, **507**, 4804
 Takhistov V., Lu P., Gelmini G. B., Hayashi K., Inoue Y., Kusenko A., 2022, *J. Cosmology Astropart. Phys.*, **2022**, 017
 Tremmel M., Kärcher M., Governato F., Volonteri M., Quinn T. R., Pontzen A., Anderson L., Bellovary J., 2017, *MNRAS*, **470**, 1121
 Trenti M., Stiavelli M., 2009, *ApJ*, **694**, 879
 Tseliakhovich D., Hirata C., 2010, *Phys. Rev. D*, **82**, 083520
 Vaskonen V., Veermäe H., 2020, *Phys. Rev. D*, **101**, 043015
 Wang F., et al., 2021, *ApJ*, **907**, L1
 Weinberger R., et al., 2018, *MNRAS*, **479**, 4056
 Weltman A., et al., 2020, *Publ. Astron. Soc. Australia*, **37**, e002
 Wilms J., Allen A., McCray R., 2000, *ApJ*, **542**, 914
 Wouthuysen S. A., 1952, *AJ*, **57**, 31
 Yuan F., Narayan R., 2014, *ARA&A*, **52**, 529
 Yuan G.-W., et al., 2023, *arXiv e-prints*, p. arXiv:2303.09391
 Zel'dovich Y. B., Novikov I. D., 1967, *Soviet Ast.*, **10**, 602
 Zhang H., Behroozi P., Volonteri M., Silk J., Fan X., Hopkins P. F., Yang J., Aird J., 2023, *MNRAS*, **518**, 2123
 Ziparo F., Gallerani S., Ferrara A., Vito F., 2022, *MNRAS*, **517**, 1086

APPENDIX A: HALO FITTING FORMULAE

The total stellar mass, as a function of redshift and halo mass, is provided by Behroozi et al. (2013, 2019, 2020); Zhang et al. (2023), based on a parametric fit to observational data. In this section, we outline how we utilize their model to calculate the total SRBH and SMBH mass within a halo.

Initially, we apply the parametric fit for a single halo accretion history, following the model detailed in the appendix of Behroozi et al. (2013). This model is initially based on the growth trajectory of the progenitor of a $10^{13} M_{\odot}$ halo, $M_{13}(z)$, and scaled to the haloes of different masses with the parametric fit. For a halo of mass M_0 (in units of M_{\odot}) at redshift $z = 0$, its progenitor mass M_h at redshift z is given by:

$$\begin{aligned}
 M_h(M_0, z) &= M_{13}(z) 10^{f(M_0, z)}, \\
 M_{13}(z) &= 10^{13.276} M_{\odot} (1+z)^{3.00} \left(1 + \frac{z}{2}\right)^{-6.11} \exp(-0.503z), \\
 f(M_0, z) &= \log_{10} \left(\frac{M_0}{M_{13}(0)} \right) \frac{g(M_0, 1)}{g\left(M_0, \frac{1}{1+z}\right)}, \\
 g(M_0, z) &= 1 + \exp \left(-4.651 \left(\frac{1}{1+z} - a_0(M_0) \right) \right), \\
 a_0(M_0) &= 0.205 - \log_{10} \left[\left(\frac{10^{9.649} M_{\odot}}{M_0} \right)^{0.18} + 1 \right].
 \end{aligned} \tag{A1}$$

For the remainder of the parametric model, we adopt the fitted parameters from Zhang et al. (2023) to ensure consistency. The star formation rate (SFR, in units of $M_{\odot} \text{yr}^{-1}$) as a function of halo mass and redshift is fitted by a double power law

$$\begin{aligned}
 \text{SFR}_{\text{SF}}(M_h, a, V_h, \epsilon_h, \alpha_h, \beta_h) &= \frac{\epsilon_h}{v_h^{\alpha_h} + v_h^{\beta_h}} M_{\odot} \text{yr}^{-1}, \\
 v_h &= \frac{v_{\text{Mpeak}}}{V_h \cdot \text{kms}^{-1}},
 \end{aligned} \tag{A2}$$

where v_{Mpeak} is the maximum velocity within a halo of mass M_h at redshift z :

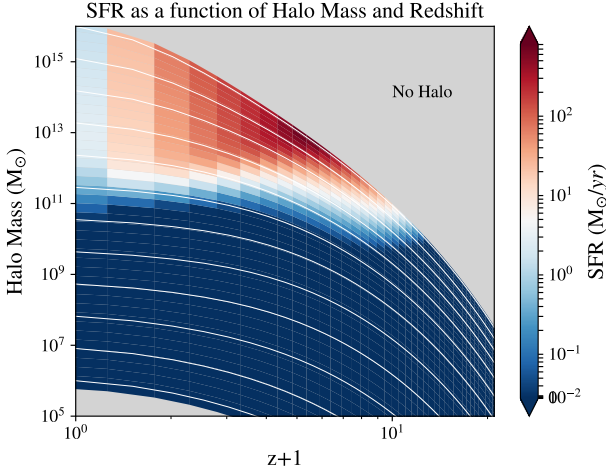


Figure A1. Star formation rate (SFR), in units of $M_{\odot} \text{ yr}^{-1}$, as a function of redshift and host halo mass, from the parametric fit generated by the UNIVERSEMACHINE (Zhang et al. 2023). Here, in addition to the overall star formation rate, we add a Pop III component as the dominant star formation process at high redshifts ($z \gtrsim 13$) (Liu & Bromm 2020a). Similar to Figure 3, the grey region represents the part of parameter space for the growth trajectories of $\gtrsim 10^{16} M_{\odot}$ haloes at $z = 0$, that are not expected to exist in the observable Universe due to low number densities. White lines represent halo growth trajectories for a single halo.

$$v_{\text{Mpeak}}(M_h, a) = 200 \text{ km s}^{-1} \left[\frac{M_h}{M_{200\text{kms}}(a)} \right]^{1/3},$$

$$M_{200\text{kms}}(a) = \frac{1.64 \times 10^{12} M_{\odot}}{\left(\frac{a}{0.378}\right)^{-0.142} + \left(\frac{a}{0.378}\right)^{-1.79}}. \quad (\text{A3})$$

Given that we have also assumed a halo growth history, this M_h will change with respect to the redshift and eventually evolve into a halo of mass M_0 at $z = 0$. The remaining parameters ($V_h, \epsilon_h, \alpha_h, \beta_h$) can be fitted with the following values:

$$\begin{aligned} \log_{10}(V_h) &= 2.289 + 1.548(a-1) + 1.218 \ln(1+z) - 0.087z, \\ \log_{10}(\epsilon_h) &= 0.556 - 0.944(a-1) - 0.042 \ln(1+z) + 0.418z, \\ \alpha_h &= -3.907 + 32.223(a-1) + 20.241 \ln(1+z) - 2.193z, \\ \beta_h &= 0.329 + 2.342(a-1) + 0.492z. \end{aligned} \quad (\text{A4})$$

Here, $a = 1/(1+z)$ is the scale factor. The resulting SFR as a function of redshift and current halo mass at redshift z is plotted as a color map in Figure A1. Since this parametric fit only provides the SFR at low redshift ($z = 0 - 10$), which corresponds to the SFR of higher metallicity stars, we also incorporate the SFR for Pop III stars from Liu & Bromm (2020a), using Equ. (23-24). We find that it generally aligns with the JWST observation of star-forming galaxies at redshift $z \simeq 10 - 16$ in terms of SFR (Harikane et al. 2023a). For higher redshifts $z \gtrsim 10$, due to the lack of data, we extrapolate the fitted star formation rate from the UNIVERSEMACHINE to approximate the stellar mass.

To calculate the SMBH mass in a halo of mass M_h at redshift $z = 1/a - 1$, we require a few additional steps. Firstly, we calculate the total stellar mass $M_{\star}(M_h, a)$ as

$$\begin{aligned} \log_{10}(M_{\star}) &= \log_{10}(\epsilon_{\star} M_1) + f \left(\log_{10} \left(\frac{M_h}{M_1} \right) \right) - f(0), \\ f(x) &= -\log_{10}(10^{\alpha_{\star} x} + 1) + \delta_{\star} \frac{(\log_{10}(1 + \exp(x)))^{\gamma_{\star}}}{1 + \exp(10^{-x})}, \end{aligned} \quad (\text{A5})$$

with fitted parameters ($v_{\star}, \epsilon_{\star}, M_1, \alpha_{\star}, \delta_{\star}, \gamma_{\star}$):

$$\begin{aligned} v_{\star} &= \exp(-4a^2), \\ \log_{10}(\epsilon_{\star}) &= -1.777 - 0.006(a-1)v_{\star} - 0.119(a-1), \\ \log_{10}(M_1) &= 11.514 + (-1.793(a-1) - 0.251z)v_{\star}, \\ \alpha_{\star} &= -1.412 + 0.731(a-1)v_{\star}, \\ \delta_{\star} &= 3.508 + (2.608(a-1) - 0.043z)v_{\star}, \\ \gamma_{\star} &= 0.316 + (1.319(a-1) + 0.279z)v_{\star}. \end{aligned} \quad (\text{A6})$$

Once we have the stellar mass for a halo at redshift z , the corresponding bulge mass M_{bulge} can be calculated using the following equations:

$$M_{\text{bulge}} = \frac{f_z(z) M_{\star}}{1 + \exp\{-1.13 [\log_{10}(M_{\star}/10^{10.2} M_{\odot})]\}}, \quad (\text{A7})$$

$$f_z(z) = \frac{z+2}{2z+2}. \quad (\text{A8})$$

Finally, $\tilde{M}_{\text{SMBH}}(M_{\text{bulge}}, \gamma_{\bullet}, \beta_{\bullet})$, the average SMBH mass corresponding to the bulge mass M_{bulge} is determined by the following fitting formula:

$$\log_{10} \tilde{M}_{\text{SMBH}} = \beta_{\bullet} + \gamma_{\bullet} \log_{10} \left(\frac{M_{\text{bulge}}}{10^{11} M_{\odot}} \right), \quad (\text{A9})$$

where

$$\begin{aligned} \gamma_{\bullet} &= 1.028 + 0.036(a-1) + 0.052z, \\ \beta_{\bullet} &= 8.343 - 0.173(a-1) + 0.044z. \end{aligned} \quad (\text{A10})$$

The resulting plot of the average SMBH mass in a given host halo of mass M_h at redshift z is given in Figure A2. When compared with the SRBH mass abundance within a halo, we find that it is smaller by at least one order of magnitude in higher mass haloes at $z \gtrsim 6$. However, the higher accretion rate for SMBHs will compensate for this difference by generating more energy feedback while growing in mass.

APPENDIX B: ACCRETING BH SPECTRA

Next, we summarize the prescription for the radiation feedback spectrum from BH accretion, as described in Takhistov et al. (2022). To streamline the analysis, we categorize the accretion process into two scenarios based on the normalized accretion factor \dot{m} : the thin-disk regime and the advection-dominated accretion flow (ADAF) regime. The former represents the case of disk formation from surrounding gas with sufficiently large angular momentum, whereas the latter implies quasi-spherical accretion where the angular velocity of the gas is smaller than the Keplerian velocity (see, e.g. Yuan & Narayan 2014).

For BH accretion in the IGM and in virialized haloes, we employ a combination of the two regimes depending on the BH accretion

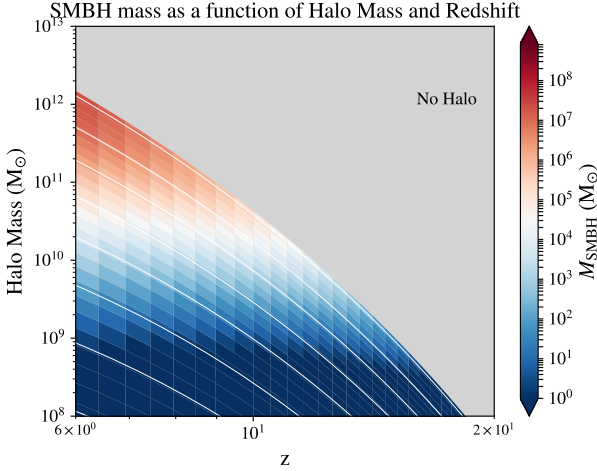


Figure A2. Average SMBH mass as a function of redshift and halo mass, from the parametric fit generated by the UNIVERSEMACHINE (Zhang et al. 2023). Here, we truncate the mass that could serve as SMBH host at $10^8 M_\odot$. Similar to Figure 3, the grey area represents the combination of parameters where no halo formation is allowed, and white lines represent individual halo growth histories.

rate¹², assuming a viscosity parameter $\alpha = 0.1$. Conversely, for SMBHs and HMXBs accreting at the Eddington rate, we assume a thin disk regime, where the blackbody spectrum is dominant.

Thin disk ($\dot{m} \geq 0.07\alpha$)

In the thin disk regime, the temperature profile of the accretion disk $T(r)$ can be modeled as a function of the radius (see also Pringle 1981):

$$T(r) = T_i \left(\frac{r_i}{r}\right)^{3/4} \left[1 - \left(\frac{r_i}{r}\right)^{1/2}\right]^{1/4}. \quad (\text{B1})$$

Here, r_i is the inner radius of the disk, which is equal to three times the Schwarzschild radius r_s . The temperature T_i at the inner radius is derived from the balance between gravitational energy release and radiative cooling:

$$T_i = \left(\frac{3GM_\bullet \dot{M}_\bullet}{8\pi r_i^3 \sigma_{\text{SB}}}\right)^{1/4} = 1.3 \times 10^3 \text{ eV} / k_B \dot{m}^{1/4} \left(\frac{M_\bullet}{10M_\odot}\right)^{-1/4}, \quad (\text{B2})$$

where σ_{SB} is the Stefan-Boltzmann constant, and k_B the Boltzmann constant.

The maximum temperature $T_{\text{max}} = T(r_{\text{max}})$ of the disk is attained at $r_{\text{max}} = 1.36r_i$, as given by the temperature profile. The minimum temperature $T_o = T(r_{\text{out}})$ is reached at the outer radius of the disk:

$$r_{\text{out}} \simeq 1.16 \times 10^{10} r_s \left(\frac{M_\bullet}{10M_\odot}\right)^{2/3} \left(\frac{v_{\text{eff}}}{10 \text{ km/s}}\right)^{-10/3}. \quad (\text{B3})$$

This outer radius is determined by equating the angular momentum of the gas from the surrounding environment to the angular momentum of the accretion disk. Here, v_{eff} is the same effective velocity as in Equ. (27).

The overall shape of the spectrum is the result of the blackbody spectrum contributing from all parts of the accretion disk, taking the following form:

¹² We note that in section 3.3 of Ricotti et al. (2008), a threshold halo mass of $\lesssim 1000M_\odot$ is introduced, below which the formation of an accretion disk is prevented.

$$L_\nu = \begin{cases} c_\alpha \left(\frac{T_{\text{max}}}{T_o}\right)^{5/3} \left(\frac{h\nu}{k_B T_{\text{max}}}\right)^2 & (\nu < k_B T_o/h) \\ c_\alpha \left(\frac{h\nu}{k_B T_{\text{max}}}\right)^3 & (k_B T_o/h < \nu < k_B T_{\text{max}}/h) \\ c_\alpha \left(\frac{h\nu}{k_B T_{\text{max}}}\right)^2 e^{1 - \frac{h\nu}{k_B T_{\text{max}}}} & (\nu > k_B T_{\text{max}}/h) \end{cases}. \quad (\text{B4})$$

Here, c_α is the normalizing flux constant such that the integration over all frequencies gives a total power of $0.057\dot{M}_\bullet c^2$, which recovers the subgrid model (Tremmel et al. 2017).

ADAF ($\dot{m} < 0.07\alpha$):

The ADAF disk dominates when the accretion rate \dot{m} is significantly sub-Eddington¹³. In this regime, we primarily consider the spectrum from the synchrotron radiation and Inverse-Compton (IC) scattering process:

$$L_\nu = \begin{cases} L_{\nu_p} \left(\frac{\nu}{\nu_p}\right)^{5/2} & (\text{Synchrotron}, \nu < \nu_p) \\ L_{\nu_p} \left(\frac{\nu}{\nu_p}\right)^{-\alpha_c} & (\text{IC}, \nu_p \leq \nu \lesssim 3k_B T_e/h) \end{cases}. \quad (\text{B5})$$

where the peak frequency ν_p is

$$\nu_p = 1.83 \times 10^3 \text{ eV} / h \\ \dot{m}^{3/4} \left(\frac{\alpha}{0.1}\right)^{-1/2} \left(\frac{1-\beta}{1/11}\right)^{1/2} \theta_e^2 \left(\frac{r_i}{3r_s}\right)^{-5/4} \left(\frac{M_\bullet}{10M_\odot}\right)^{-1/2}, \quad (\text{B6})$$

and the corresponding peak luminosity:

$$L_{\nu_p} = 5.06 \times 10^{37} \frac{\text{erg}}{\text{s} \cdot \text{eV}/h} \dot{m}^{3/2} \alpha^{-1} (1-\beta) \theta_e^5 \left(\frac{r_i}{r_s}\right)^{-1/2} \left(\frac{M_\bullet}{10M_\odot}\right). \quad (\text{B7})$$

To ensure overall consistency, we normalize the product of the peak frequency and luminosity, $\nu_p L_{\nu_p}$, with the results from Equ. (44).

In these equations, β is a partition parameter for total pressure originating from the gas and magnetic field, with values equaling 10/11. θ_e is the dimensionless electron temperature written in units of electron rest mass m_e :

$$\theta_e = \frac{k_B T_e}{m_e c^2} = \frac{T_e}{5.93 \times 10^9 \text{ K}} \\ \simeq 0.17 A_c^{-1/7} \delta^{1/7} \alpha^{3/14} (1-\beta)^{-1/14} \left(\frac{r_i}{r_s}\right)^{3/28} \left(\frac{M_\bullet}{10M_\odot}\right)^{1/14} \dot{m}^{-5/28}, \quad (\text{B8})$$

where $A_c^{-1/7}$ is a pre-factor related to the relative contribution of IC to the total power depending on the accretion rate. Since we do not further divide the ADAF case, we will assume a uniform value of 1.1. δ is the electron heating efficiency approximated by a value of 0.3.

The exponent α_c for the IC part of the spectrum in Equ. (B5), is determined by the following expression:

$$\alpha_c = -\frac{\ln \tau_{\text{es}}}{\ln A}, \quad (\text{B9})$$

where $\tau_{\text{es}} = 12.4 \dot{m} \alpha^{-1} (r_i/r_s)^{-1/2}$ is the optical depth for electron scattering, and $A = 1 + 4\theta_e + 16\theta_e^2$ is the amplification factor. Typically, for a $10M_\odot$ BH that accretes at a rate of $\dot{m} \sim 10^{-6}$, this exponent will yield a value of $\alpha_c \sim 2$, where the slope becomes asymptotically flatter with increasing accretion rate \dot{m} and BH mass

¹³ For a complete derivation, see e.g. Narayan & Yi (1995).

M_\bullet . When the accretion is efficient, reaching the critical limit for the thin disk of regime $\dot{m} \sim 10^{-2}$, for the same BH mass of $10 M_\odot$, the power-law exponent approaches $\alpha_c \sim 1$.

APPENDIX C: PBH ACCRETION ENHANCED BY HALO CLOTHING

In this section, we summarize the changes to the accretion factor when PBHs are clothed by haloes, following the work of Ricotti (2007); Mack et al. (2007); Ricotti et al. (2008); De Luca et al. (2020a). We define a parameter κ as the ratio of the Bondi radius to the radius of the clothed halo:

$$\kappa = 2.2 \times 10^{-3} \left(\frac{1+z}{1000} \right) \left(\frac{M_h}{M_\odot} \right)^{\frac{2}{3}} \left(\frac{v_{\text{eff}}}{10 \text{ km s}^{-1}} \right)^{-2}. \quad (\text{C1})$$

Here, M_h is the halo mass seeded by PBHs, given by $M_h \sim M_c (1 + z_{\text{eq}})/(1+z)$. In our case, since we choose the characteristic PBH mass to be smaller than $\sim 100 M_\odot$, we estimate $\kappa < 2$ for $z \gtrsim 30$. The original scale parameter, λ , in the relevant equations for the accretion rate, Equ. (30) to (32), is modified as follows:

$$\lambda^h \equiv \bar{\Gamma}^{\frac{2-\hat{\alpha}}{\hat{\alpha}-1}} \lambda(\hat{\beta}^h), \quad \hat{\beta}^h \equiv \kappa^{\frac{2-\hat{\alpha}}{\hat{\alpha}-1}} \hat{\beta}, \quad (\text{C2})$$

where $\hat{\alpha}$ is the power of the surrounding density profile, and

$$\bar{\Gamma} = \left(1 + 10 \hat{\beta}^h \right)^{\frac{1}{10}} \exp(2 - \kappa) \left(\frac{\kappa}{2} \right)^2. \quad (\text{C3})$$

Here we adopt $\hat{\alpha} = 2.2$, consistent with the density profiles in the simulations by Liu et al. (2022) and similar to the value $\hat{\alpha} = 2.25$ adopted in Ricotti et al. (2008) for the Bertschinger self-similar solution. Furthermore, we use the corrected accretion parameters λ^h and $\hat{\beta}^h$ to replace the value of λ and $\hat{\beta}$ in Equ. (30) and (31).

On the other hand, at $z \lesssim 30$, we find $\kappa \gtrsim 2$, which means the DM halo behaves similarly to a point mass of M_h . Therefore, we will apply a correction to Equ. (30) as:

$$\dot{m} = 0.042 \lambda \left(\frac{1+z}{1000} \right) \left(\frac{M_\bullet}{10 M_\odot} \right) \left(\frac{v_{\text{eff}}}{10 \text{ km s}^{-1}} \right)^{-3}, \quad (\text{C4})$$

using the original equations, Equ. (31) and (32) to calculate the accretion constant λ . To evaluate the energy density, we consider contributions from BHs residing in different environments. However, distinguishing between accretion in the IGM versus accretion in halo environments is challenging, especially at redshifts $z \gtrsim 30$. To tentatively make this distinction, we set the same mass boundary $M_{\text{min}} = \max(M_c \Omega_m / f_{\text{PBH}} \Omega_{\text{DM}}, M_{\text{vir}}, M_c (1 + z_{\text{eq}})/(1+z))$, distinguishing virialized haloes that could host more than one PBH from those seeded by a single PBH. We treat the latter case similarly to the IGM case but calculate it using the enhanced accretion rate. More simulation work is needed in the future to better address the effects of PBH halo seeding.

Our results, plotted in Figure C1, are compared with the energy density from PBHs in Figure 5. We find that the enhancement in accretion could increase the total energy output by an order of $\sim O(10^4)$ at $z \lesssim 30$, which would imply more stringent constraints when comparing the intensity output from PBHs to the radiation background limits.

This paper has been typeset from a \LaTeX file prepared by the author.

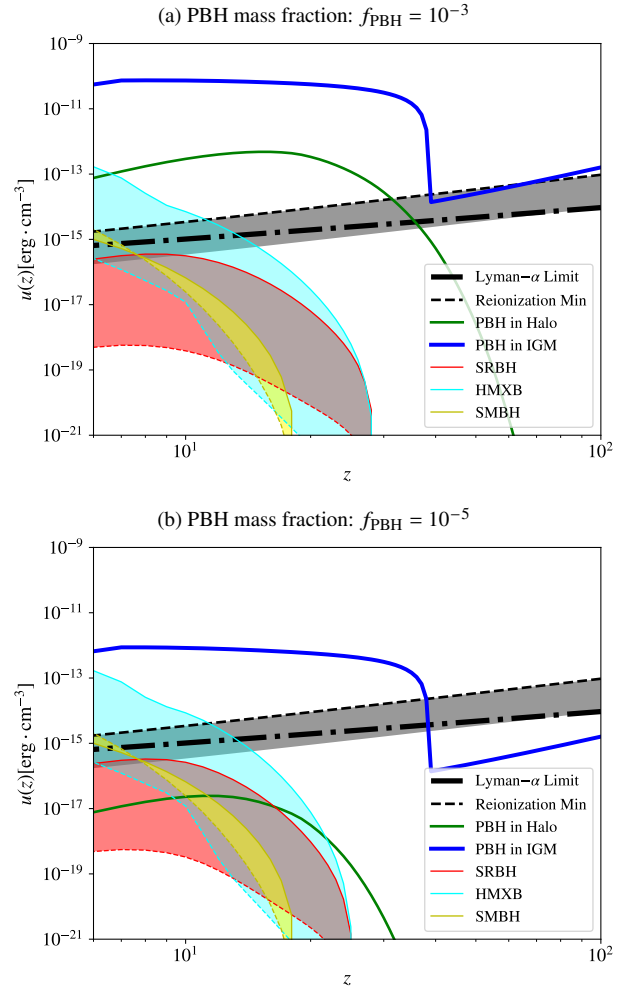


Figure C1. Effect of enhanced accretion in PBH-seeded haloes. Similar to Figure 5, we show here the integrated (bolometric) energy density from BH accretion feedback of different origins vs. redshift: PBHs in the IGM (blue), in haloes (green), SRBHs (red), HMXBs (cyan), and SMBHs (yellow). For PBHs, we assume a monochromatic mass distribution with $M_c = 10 M_\odot$, and mass fractions of $f_{\text{PBH}} = 10^{-3}$ (upper panel) and 10^{-5} (lower panel). Here, we consider the same range for the abundance of BHs as shown in Figure 4, when deriving possible radiation outputs, but include the effect of halo enhancement on PBH accretion.